Spatial Patterns of Sandy Beaches in China and Risk Analysis of Human Infrastructure Squeeze Based on Multi-Source Data and Ensemble Learning

Jie Meng[1,2], Duanyang Xu[1], Zexing Tao[1], Quansheng Ge[1]

[1]Key Laboratory of Land Surface Pattern and Simulation, Institute of Geographic Sciences and Natural Resources Research, Chinese Academy of Sciences, Beijing 100101, PR China

[2]University of Chinese Academy of Sciences, Beijing 100049, PR China

Correspondence to: Duanyang Xu (Xudy@igsnrr.ac.cn)

Abstract. Sandy beaches provide essential ecological and economic services, but their functions are increasingly threatened by human activities. Analyzing the spatial distribution of China's sandy beaches and the impacts of human activities offers valuable insights for coastal resource management and ecological protection. However, remote sensing technologies face challenges such as limited data sources and tidal influences, which affect recognition accuracy. Therefore, integrating multi-source remote sensing data and reducing the impact of tidal fluctuations to improve recognition accuracy remains a key challenge. This study proposes an innovative approach utilizing multi-source data and an ensemble learning model to identify sandy beaches in China (2016–~~2023~~2024). By integrating Sentinel-1/2 satellite data, terrain data, and nighttime light data, along with spectral, index, terrain, texture, and polarization features, sandy beaches were identified across multiple years, and the results were consolidated into a single-year dataset to analyze spatial patterns and risks from human infrastructure squeeze. (1) High-precision classification identified ~~2984~~3347 sandy beaches in China, covering a total area of ~~260.70~~320.50 km². Guangdong had the largest number, area, and perimeter, while ~~Shanghai~~ Hebei had the widest sandy beaches. (2) In Fujian, Guangdong, and Taiwan, the identified sandy beaches covered 180.05~~149.68~~ km², with perimeters of 5610.26~~5155.91~~ km and widths of 54.91~~49.50~~ m, 38.92~~32.83~~ m, and 57.17~~50.70~~ m, respectively. These results were significantly better than those from ~~published reference~~ datasets. (3) From 1990 to ~~2023~~2024, the area at risk from human infrastructure squeeze increased from 134.39~~109.95~~ km² to 181.42~~245.58~~ km², a rise of 47.03~~135.63~~ km², with the most significant increase occurring between ~~1990~~1995 and 2000. Guangdong and Fujian showed growth rates of 0.38~~1.05~~ km²/year and 0.32~~0.73~~ km²/year, respectively. This study provides an up-to-date dataset on China's sandy beaches. It assesses their spatial patterns and human impact risks, contributing to research and policy for the sustainable development of coastal zones (https://doi.org/10.5281/zenodo.15307240, Meng et al., 2025).

1 Introduction

As transitional zones between land and sea, sandy beaches play a critical ecological role, providing essential habitats for various flora and fauna and offering crucial ecosystem services such as climate regulation, wave attenuation, and storm surge protection (Temmerman et al., 2013; Lansu et al., 2024; Mentaschi et al., 2018). Moreover, sandy beaches support a wide range of economic activities including tourism, fisheries, marine resource development, and land use, thereby holding considerable economic value (Mejjad et al., 2022; Brščić et al., 2020; Ranasinghe et al., 2016). However, with the development of coastal areas, sandy beach ecosystems are increasingly threatened by human activities. Urban expansion, pollution, and tourism-related disturbances have transformed many natural sandy beaches into residential, commercial, or industrial land, leading to habitat degradation and the loss of ecological functions (Lu et al., 2018; Barbier et al., 2011). Therefore, accurate identification and mapping of sandy beach areas are essential for ecological conservation, resource management, and sustainable coastal development.

Efficient and precise identification of sandy beach areas is a core component of sandy beach research (Ponte et al., 2016). Traditional field-based surveys, while offering high accuracy, are often constrained by high labor costs, low efficiency, and environmental limitations (Rodríguez-Padilla et al., 2024; Valderrama-Landeros et al., 2022; Bai et al., 2021; Blenkinsopp et al., 2021). In contrast, remote sensing technologies based on satellites, unmanned aerial vehicles (UAVs), or aerial platforms, with their high temporal resolution and broad spatial coverage, enable effective data acquisition across different regions and climatic conditions and thus have become the primary method for large-area sandy beach identification (Xu et al., 2024; Sun et al., 2024; Salameh et al., 2024; Nativí-Merchán et al., 2024; Splinter et al., 2018). Current remote sensing-based sandy beach identification methods are generally categorized into visual interpretation and automated classification (Sekovski et al., 2014; Toure et al., 2019). While visual interpretation relies heavily on expert experience and high-quality imagery, it is susceptible to tidal variations and subjectivity, making it unsuitable for large-area or long-term monitoring. Automated classification methods, on the other hand, extract features such as spectral and texture information to achieve more consistent and efficient identification, gradually becoming the mainstream approach in remote sensing-based sandy beach studies. These methods are particularly suited for large-area monitoring, providing efficient and accurate results over extensive areas (Masria et al., 2024; Yasir et al., 2020; Wei et al., 2021).

Currently, remote sensing-based automated sandy beach recognition methods encompass a variety of techniquestechnologies, including threshold segmentation, machine learning methods, and deep learning methods (Sekar et al., 2020; Vicens-Miquel et al., 2022; Rabehi et al., 2021). Threshold segmentation divides the image into sandy beach and non-sandy beach areas by analyzing pixel value thresholds of remote sensing images. This method is simple and efficient, but the segmentation performance is often poor in complex backgrounds or areas with subtle grayscale differences (Bao et al., 2018). Machine learning and deep learning methods are similar in principle, as both build classification models through training datasets, enabling them to handle complex images and exhibit strong pattern recognition capabilities. Machine learning methods typically require integrating multiple features from remote sensing images, such as spectral, spatial, and texture information,

while deep learning methods automatically extract features and perform classification using multi-layer neural networks, capable of handling large-scale and complex datasets. For example, Latella et al. conducted a exploratory~~rough~~ survey and monitoring of sandy beaches by comparing Sentinel-2 and Landsat images, using random forests and various spectral indices (Latella et al., 2021); while Yong et al. used a binary image segmentation method based on the U-Net model in convolutional neural networks to accurately delineate the sandy beach outline of the southeastern coast of Australia (Yong et al., 2024).
65 Despite significant progress in improving recognition accuracy and spatial scalability, machine learning and deep learning methods still face several challenges under complex conditions and tidal interference. Specifically, due to the single spectral feature of optical imagery, the recognition accuracy of machine learning methods still needs improvement in certain situations, particularly in areas where feature boundaries are unclear or the background is complex. For deep learning methods, the
70 influence of tidal variations remains a significant challenge. To overcome the impact of tidal variations on sandy beach extraction from remote sensing images~~tidal image interference~~, multi-year data needs to be introduced, which requires a large amount of labeled data for training. However, high-quality labeled data is~~are~~ often difficult to obtain, and the training process is time-consuming, increasing computational resource consumption. Moreover, during the training of multi-layer neural networks, overfitting may also become an issue (Zhu et al., 2023; Chen et al., 2018; Zhou et al., 2023; Wang et al., 2024).
75 The coastal regions of China are among the most economically developed and dynamic areas in the country, encompassing several key economic belts and contributing to over~~contributing over~~ 57% of the national gross income (Tian et al., 2016; Wang et al., 2024; Feng et al., 2025). These areas not only have a solid industrial foundation, vibrant trade, and advanced service sectors but also serve as the core engines of national economic growth. However, despite the rapid economic development in these regions, there is a lack of nationwide dynamic monitoring tools for sandy beaches, and the risks posed
80 by human infrastructure squeeze—particularly due to urban development and coastal expansion—are not well understood. Past research has mainly relied on single optical imagery data and has not fully considered the use of multi-year data to address tidal changes, which limits the comprehensive understanding and monitoring of coastal beach changes. To address these challenges, this study is divided into two main components: (1) This study proposes a novel method for sandy beach identification using multi-source remote sensing and ensemble learning. Sentinel-1/2 imagery, nighttime light, and terrain data are integrated to extract spectral, index, terrain, polarization, and texture features. A stacking ensemble framework enhances
85 classification accuracy and robustness. Multi-year sandy beach data extracted using ensemble learning~~Multi-temporal data~~ from 2016 to 2023~~2024~~ are merged to construct~~used to~~ build an annual representative sandy beach dataset, reducing tidal fluctuation impacts and supporting precise mapping and monitoring; (2) Based on human infrastructure data~~this dataset~~, buffer zones are created and combined with this dataset~~human infrastructure data~~ to identify areas at risk of encroachment. Spatial
90 analysis evaluates anthropogenic pressure on beaches across regions. The results offer a scientific basis for delineating ecological red lines and inform strategies for beach conservation and coastal zone management.

2 Study area and materials

2.1 Study area

To identify sandy beaches along China's coast from 2016 to ~~2023~~2024, this study adopts the ~~2023~~ 2024 coastline of China as the baseline. A buffer zone extending 10 km inland and 20 km offshore is applied to ensure the integrity of the sandy beach area (Li et al., 2022). The study area spans from 107°54'E to 124°21'E longitude and from 17°58'N to 41°8'N latitude, encompassing 14 regions (Liaoning, Hebei, Shandong, Jiangsu, Zhejiang, Fujian, Guangdong, Hainan, Taiwan, Guangxi, Tianjin, Shanghai, Hong Kong, and Macao) (Fig. 1). For statistical convenience, the coastal regions of Hong Kong and Macao are included within the Guangdong coastal region.
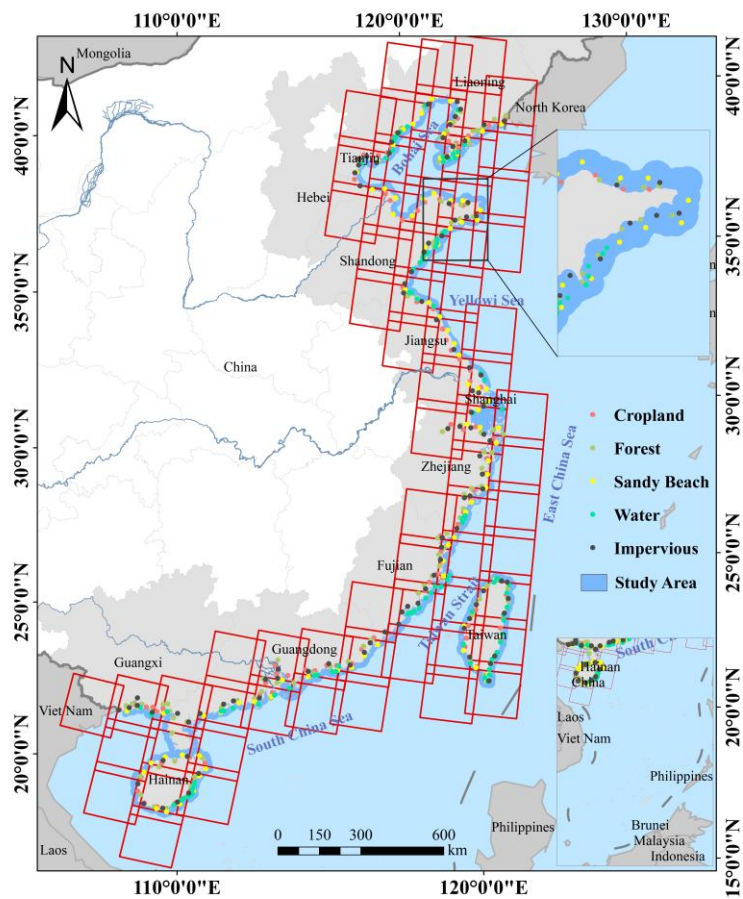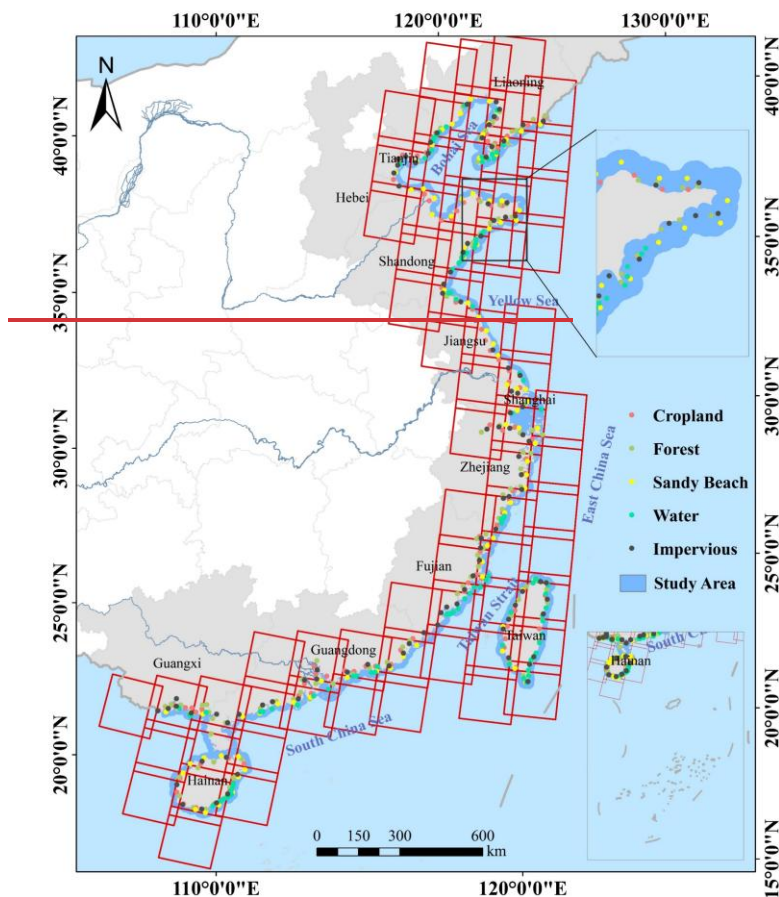
Figure 1: Location of China's coastal zone and distribution of ==partial typical land feature points~~partial test points~~== for ==result==s verification.

设置了格式: 突出显示
设置了格式: 突出显示
设置了格式: 字体: Times New Roman, 突出显示

2.2 Remote sensing data

105   This study used Sentinel-1, Sentinel-2, and Google Earth imagery, with data collected from January 1, 2016, to December 31, ==~~2023~~2024==. The Sentinel-1 images are Level-1 Ground Range Detected (GRD) products, acquired in Interferometric Wide (IW) mode, including dual-polarization VV (vertical transmit, vertical receive) and VH (vertical transmit, horizontal receive) data

(Tian et al., 2022). A total of 23859 Sentinel-1A images were selected, and annual mean composites were generated for each polarization channel (Fig. 2a). For Sentinel-2, five spectral bands were used: four visible and near-infrared bands (Bands

110 2, 3, and 8) with a resolution of 10 m, and one shortwave infrared band (Band 11) with a resolution of 20 m. A total of 80759 L2A and L1C images were selected, with cloud cover below 20% (Fig. 2b) (Li et al., 2022). After atmospheric correction, the QA60 quality band was applied to remove clouds and cloud shadows. Since atmospheric correction is not essential for applications not involving complex spectral analysis, L1C images were used for years lacking L2A data (Wang et al., 2023). Finally, cloud-free median composites were generated and resampled to a 10 m resolution. Google Earth imagery

115 was sourced from the "Google Earth Engine" plugin and online map services on the QGIS platform, with a spatial resolution of 1 to 5 m, enabling clear visualization of beach areas with high geographical accuracy and temporal consistency.
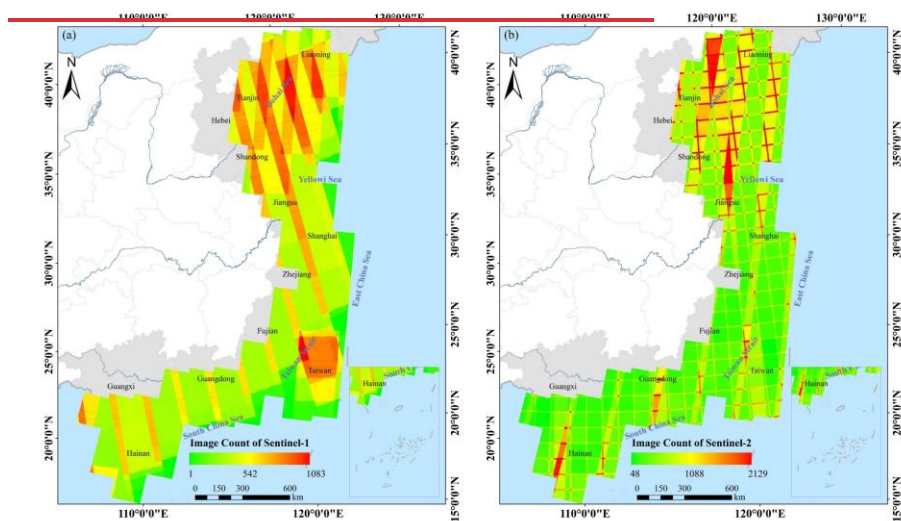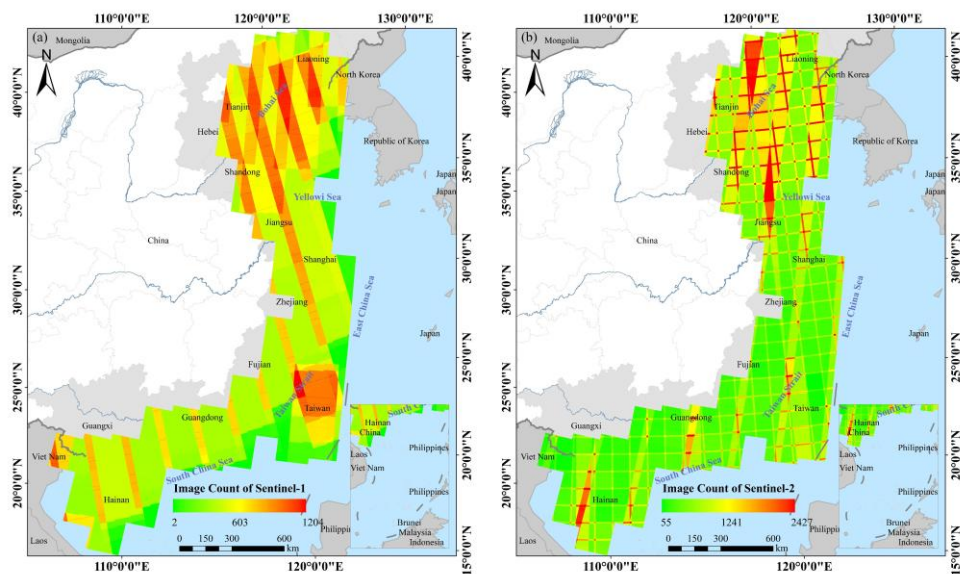
Figure 2: Spatial distribution of Sentinel-1 and Sentinel-2 images used in this study from 2016 to 2024: (a) Image Count of Sentinel-1, (b) Image Count of Sentinel-2.

2.3 Other data

The NASADEM dataset, provided by NASA and based on C-band radar with a 30 m resolution, accurately reflects global elevation. This study used the 2000 NASADEM data, resampled to 10 m, as terrain data for the period from 2016 to 20232024. VIIRS nighttime light data, provided by NOAA and NASA with a 500 m resolution, were used to represent global nighttime illumination. The data from 2016 to 2023 2024 were selected, resampled to 10 meters, clipped to [0, 63] to remove outliers, normalized, and then used as the nighttime light dataset for this study. The land cover data selected for this study is the Landsat-derived annual China Land Cover Dataset (CLCD) from 1990 to 20232024, with a resolution of 30 m, used to study changes in the area of human infrastructure squeeze risk (Yang et al., 2021). The per capita GDP, resident population, built-up area, and road area of the study area from 1990 to 2023 2024 were obtained from the National Bureau of Statistics and local statistical bureaus (https://www.stats.gov.cn/). In addition, data from 1990, 2000, 2010, and 2020 were extracted for Jinjiang, Licheng, and Fengze Districts of Quanzhou City to assess human infrastructure squeeze risk. GDP and population density data were obtained from the China GDP and Population Spatial Distribution Kilometer Grid Datasets (Xu et al., 2017). Built-up area data were sourced from the GHS-BUILT-H R2023A dataset published by the European Commission Joint Research Centre in 2022 2023 2024 (Pesaresi et al., 2023). Road network data were derived from the national basic geographic information data (https://www.webmap.cn/) and Harvard University (Baum-Snow et al., 2017). If data for a specific year were unavailable, the data from the nearest available year were used instead.

2.4 PublishedReference datasets

In this study, we used three datasets to evaluate our identified sandy beach dataset (Table 1): (1) The China sandy beach dataset, data directly obtained from the OpenStreetMap (OSM) database;The 2023 China sandy beach dataset identified through visual interpretation of Sentinel-2 and Google Earth imagery; (2) The 2022 China 10m sandy beach dataset identified by Ni et al. (Ni et al, 2024) using a support vector machine method based on Sentinel-2 imagery; (3) The 2020 China coastal land use dataset at 10m resolution, identified by Miao et al. (MiaoLi et al, 2022) using an object-oriented classification method based on Sentinel-2 imagery.

Table 1: Datasets used to evaluate the accuracy of sandy beach classification.

Datasets	Time	Spatial resolution	Dataset source	References
Dataset 1	\2023	\	https://download.geofabrik.de/derived from our visual interpretation	\
Dataset 2	2022	10m	https://zenodo.org/records/14051471	Ni et al. (2024)
Dataset 3	2020	10m	http://fuselab.hku.hk	Miao et al. (2022)

3 Methodology~~Study area and materials~~

To accurately monitor the current status of sandy beaches in China, this study integrates multi-source data from 2016 to ~~2023~~2024, including Sentinel-1/2 imagery, terrain data, and nighttime light data. By processing these multi-source datasets, spectral, index, terrain, texture, and polarization features were extracted to construct a multi-source, multi-feature, and multi-model framework based on a stacking ensemble learning approach, aiming to delineate the spatial distribution of sandy beaches in China. On this basis, 100 m buffer zones were established based on impervious surface data from 1990 to 2024 and combined with the sandy beach dataset~~by combining existing impervious surface data from 1990 to 2023, 100 m buffer zones were established~~ for overlay analysis to identify areas at risk of human infrastructure squeeze and to analyze their spatiotemporal dynamics. The technical framework of the study is illustrated (Fig. 3).
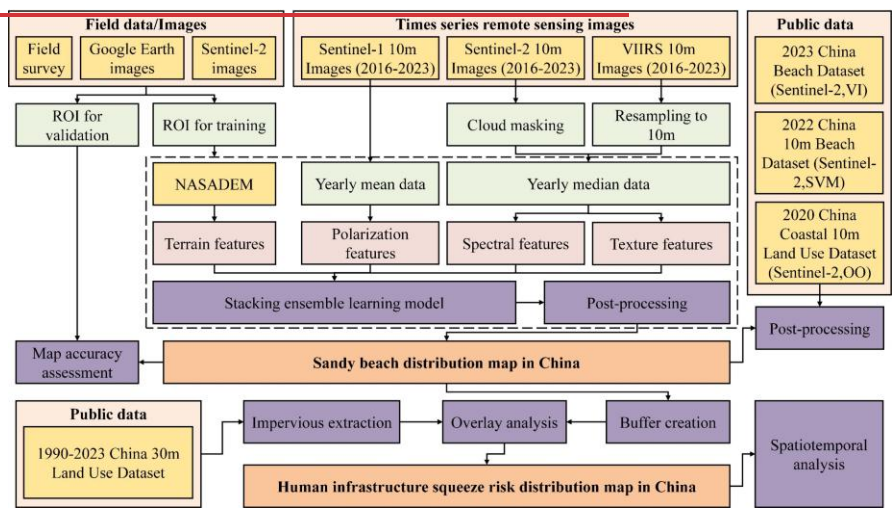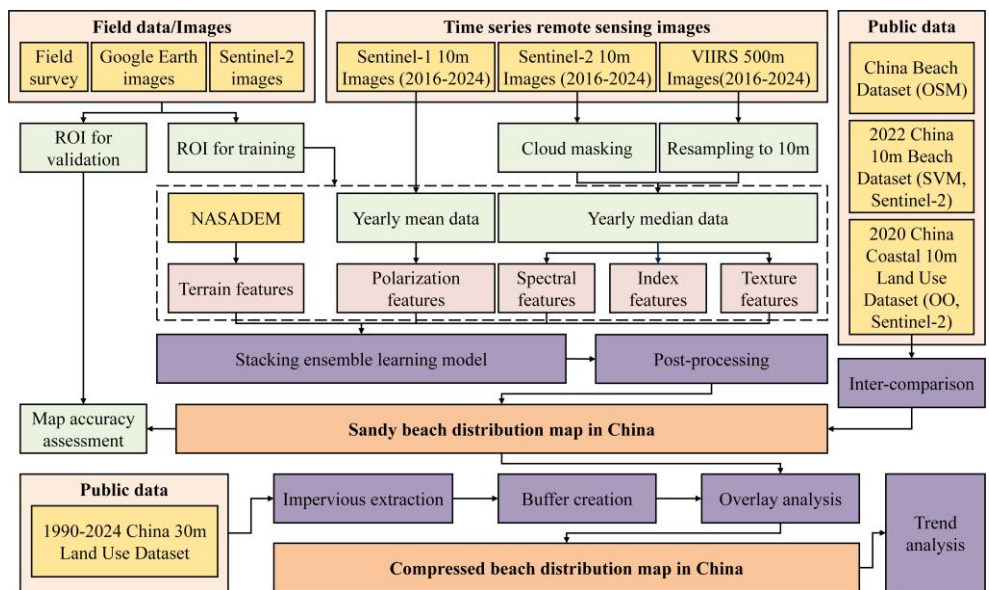
Figure 3: ~~The technical framework of the study~~Spatial distribution of Sentinel-1 and Sentinel-2 images used in this study: (a) Image Count of Sentinel-1, (b) Image Count of Sentinel-2.

3.1 Sample generation via visual interpretation

The main land cover types in the non-beach areas of the study area include farmland, forest, water, and impervious, which are defined based on typical coastal land cover characteristics in China (Yang et al., 2021). In the sample library, these non-sandy beach types, in addition to the sandy beach samples, play an important role. Therefore, we define the land use types in the study area as ~~sandy beaches and non-sandy beaches, with non-sandy beach types including farmland, forest, water, and impervious.~~farmland, forest, water, impervious, and sandy beaches. Based on field surveys, we conducted annual visual interpretation using Google Earth and Sentinel-2 imagery to label samples from 2016 to ~~2023~~2024. Through this approach, a candidate sample library was built, containing ~~47,937~~341057 samples, with ~~33,243~~249098 for model training and ~~14,694~~91959 for testing (Fig. 4).
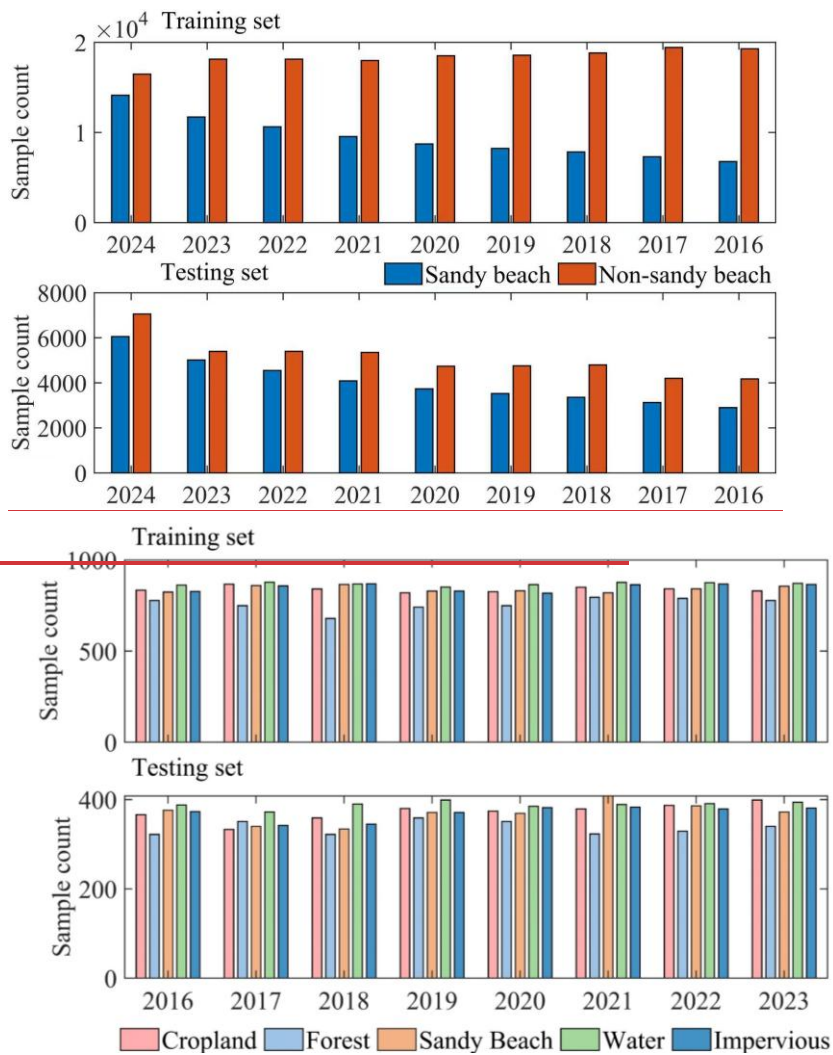
Figure 4: Training and testing sets.

3.2 Constructing sandy beach classification input features using multi-source data

This study selected 24 indicators from ~~four~~ five dimensions—spectral, index, terrain, polarization, and texture—as input features for the ensemble learning model (Table 2). First, the VV and VH polarization modes were selected as polarization features. Next, five bands—Band 2, Band 3, Band 4, Band 8, and Band 11—were chosen as spectral features, while eight indices—NDWI, NDVI, NDSI, NDBI, EVI, SAVI, BSI, and NDUI—were treated as index features.~~along with eight spectral indices—NDWI, NDVI, NDSI, NDBI, EVI, SAVI, BSI, and NDUI—were chosen as spectral features.~~ Then, grayscale images were generated using Band 3, Band 4, and Band 8, and six texture metrics—contrast, correlation, variance, angular second moment, inverse difference moment, and entropy—were derived from the grayscale images as texture features. Finally, elevation, slope, and aspect were selected as terrain features.

Table 2: Input features for sandy beach classification.

Features	Indices	Definition	Reference
Polarization (P)	Polarization bands	VV, VH	Jiang et al., 2023
Spectral (S)	Spectral bands	Band2, Band3, Band4, Band8, Band11	Nemmaoui et al., 2015
Index (I)	Normalized Difference Water Index (NDWI)	(Band3 - Band8) / (Band3 + Band8)	Zou et al., 2018
	Normalized Difference Vegetation Index (NDVI)	(Band8 – Band4) / (Band8 + Band4)	Pickens et al., 2020
	Normalized Difference Snow Index (NDSI)	(Band3 – Band11) / (Band3 + Band11)	Xiao et al., 2024
	Normalized Difference Built-up Index (NDBI)	(Band11 – Band8) / (Band11 + Band8)	Zhang et al., 2023
	Enhanced Vegetation Index (EVI)	2.5 * (Band8 – Band4) / (Band8 + 6 * Band4 - 7.5 * Band2 + 1)	Jiang et al, 2023
	Soil Adjusted Vegetation Index (SAVI)	1.5 * (Band8 – Band4) / (Band8 + Band4 + 0.5)	Rhyma et al., 2020
	Bare Soil Index (BSI)	((Band4 + Band11) - (Band8 + Band2)) / ((Band4 + Band11) + (Band8 + Band2))	Roy et al, 1996
	Normalized Difference Urban Index (NDUI)	(VNTL - NDVI) / (VNTL + NDVI)	Zhang et al., 2015
Texture (T)	Grayscale images(Gray)	0.3 * Band8 + 0.59 * Band4 + 0.11 * Band3	Tassi et al, 2020

Features	Indices	Definition	Reference
	Contrast (Con) (GLCM 3×3)	$\sum_{i,j} (i-j)^2 \cdot P(i,j)$	
	Correlation (Cor) (GLCM 3×3)	$\sum_{i,j} \dfrac{(i \cdot j \cdot P(i,j) \cdot \mu_x \cdot \mu_y)}{\sigma_x \cdot \sigma_y}$	
	Variance (Var) (GLCM 3×3)	$\sum_{i,j} (i-\mu)^2 \cdot P(i,j)$	
	Angular Second Moment (ASM) (GLCM 3×3)	$\sum_{i,j} P(i,j)^2$	
	Inverse Difference Moment (IDM) (GLCM 3×3)	$\sum_{i,j} \dfrac{P(i,j)}{1+(i-j)^2}$	
	Entropy (Ent) (GLCM 3×3)	$-\sum_{i,j} P(i,j) \cdot \log(P(i,j))$	
Terrain (Tr)	Terrain factors	Elevation, Slope, Aspect	Lin et al, 2021

3.3 Sandy beach classification using an ensemble learning model

Stacking is a powerful ensemble learning method that uses predictions from multiple base learners as inputs to a meta-learner for final prediction. It combines the strengths of different models to overcome individual limitations, enhancing accuracy, stability, and generalization (Chen et al., 2024). In this study, Random Forest (RF), Gradient Boosting Decision Tree (GBDT)~~Support Vector Machine (SVM)~~, eXtreme Gradient Boosting (XGB)~~Classification and Regression Tree (CART)~~, and Light Gradient Boosting Machine (LGBM)~~Gradient Boosting Decision Tree (GBDT)~~ were selected as base learners. Their output classification probabilities were used as input features for the meta-learner, which adopted Logistic Regression (LR)~~the Minimum Distance (MD) method~~ to integrate probabilities, calculate distances to target classes, and produce final results (Table 3). For performance comparison, Support Vector Machine (SVM), K-Nearest Neighbor (KNN), RF, Classification and Regression Tree (CART), and Convolutional Neural Network (CNN) models were also employed as benchmark models.

Table 3: Parameters of base models

Classifier	Definition
RF	n_estimators=100, random_state=42~~NumberOfTrees=100, minLeafCount=1, bagFraction=0.5~~
GBDT~~SVM~~	n_estimators=100, random_state=42~~KernelType='RBF', cost=1, degree=3~~
XGB~~CART~~	n_estimators=100, random_state=42~~MinLeafCount=1~~
LGBM~~GBDT~~	n_estimators=100, random_state=42~~NumberOfTrees=100, maxDepth=5, minLeafCount=1, learningRate=0.1~~
LR~~MD~~	\

3.4 Model results processing and analysis

3.4.1 Post-processing

Pixel-based classification algorithms inevitably produce salt-and-pepper noise because sandy beaches share similar spectral characteristics with certain areas, such as buildings and bare land, making them difficult to distinguish~~Pixel-based classification algorithms inevitably produce salt-and-pepper noise, and some small patches—such as buildings and bare land—are difficult to distinguish from environmentally influenced sandy beaches~~ (Mattson et al., 2024). To reduce noise and remove isolated areas, we applied spatial filtering and connectivity analysis. A 100 m coastal buffer based on administrative boundaries was used to clip and filter non-sandy beach areas. Based on sandy beach patches, holes smaller than 2000 m² (20 pixels) were filled, and sandy beach patches smaller than 1000 m² (10 pixels) were removed.~~We filled sandy beach patches smaller than 2000 m² (20 pixels) and removed those smaller than 1000 m² (10 pixels).~~ Finally, the sandy beach boundaries were refined through a thorough review and manual interpretation based on visual assessment.

3.4.2 Accuracy assessment

This study assessed the accuracy of sandy beach classification results using ~~14,694~~91959 test samples from 2016 to ~~2023~~2024, calculating Accuracy~~Producer's Accuracy (PA)~~, Precision~~User's Accuracy (UA)~~, Recall~~Kappa coefficient~~, sandy beach F1-score~~Overall Classification Accuracy (OA)~~, and Area Under the Curve (AUC)~~sandy beach F1-score~~ through the confusion matrix (Table 4).

Table 4: Accuracy assessment metrics

Assessment indicators	Definition	Reference
Accuracy~~PA~~	$Accuracy = \dfrac{TP+TN}{TP+TN+FP+FN}$ ~~$PA_i = \dfrac{TP_i}{TP_i + FN_i}$~~	Wang et al., 2023~~Cao et al., 2021~~
Precision~~UA~~	$Precision = \dfrac{TP}{TP+FP}$ ~~$UA_i = \dfrac{TP_i}{TP_i + FP_i}$~~	Zhang et al., ~~2022~~2024
Recall~~Kappa Coefficient~~	$Recall = \dfrac{TP}{TP+FN}$ ~~$Kappa = \dfrac{P_0 - P_e}{1 - P_e}$~~	~~Zhang~~Pan et al., ~~2020~~2019
F1-score~~OA~~	$F1\text{-}score = 2 \times \dfrac{Precision \times Recall}{Precision + Recall}$ ~~$OA = \dfrac{\sum TP_i}{\sum TP_i + \sum FP_i + \sum FN_i + \sum TN_i}$~~	Fu et al., 2021~~Wang et al., 2023~~
AUC~~F1-score~~	$AUC = \int_{0}^{1} TPR\, d(FPR)$ ~~$F1_i\text{-}score = \dfrac{2 \cdot TP_i}{2 \cdot TP_i + FP_i + FN_i}$~~	~~Fu~~Liao et al., ~~2021~~2025

3.4.3 Analysis of human infrastructure squeeze risk trends

Approximately 33% of global sandy beaches lack more than 100 meters of infrastructure-free space, and in this study, human infrastructure squeeze risk is defined as the risk that occurs when infrastructure (such as buildings, roads, ports, etc.) is located within 100 meters of a sandy beach area. This threshold was chosen because infrastructure within this range can significantly impact the sandy beach area, leading to changes in its size or degradation of the ecosystem (Lansu et al., 2024). Therefore, this study established a 100-meter buffer zone around the Chinese land use dataset~~established a 100 m buffer zone around the sandy beach area in China~~ and conducted an overlay analysis using the obtained sandy beach data~~impervious surface data from the Chinese land use dataset~~. The analysis generated annual human infrastructure squeeze risk areas to evaluate the squeeze effects of infrastructure on sandy beaches from 1990 to ~~2023~~2024. To further quantify the spatiotemporal changes in human infrastructure squeeze risk areas across regions, the study applied the Sen's slope method to calculate trend values (Zhang et al., 2023; Qiao et al., 2025). By applying this method, the study quantified the annual change rate and long-term trend of the risk zones across different regions~~risk areas across regions~~ from 1990 to ~~2023~~2024.

4 Results and analysis

4.1 Accuracy Assessment and Mapping of Chinese Sandy Beaches

The ensemble learning algorithm's performance was evaluated using key metrics such as Accuracy, Precision, Recall, sandy beach F1-score, and AUC, with the results presented in Table 5. ~~The performance of the ensemble learning algorithm was validated by calculating PA, UA, F1-score, OA, and Kappa coefficient, and we obtained the validation results (Table 5).~~ From 2016 to ~~2023~~2024, all classification results had values above ~~0.90~~0.85 for these metrics, with the best results in ~~2024~~2017, confirming the algorithm's stability, reliability, and accuracy in sandy beach classification.

Table 5: Accuracy assessment of ensemble learning results

Year	Accuracy~~PA~~	Precision~~UA~~	Recall~~F1-score~~	F1-score~~OA~~	AUC~~Kappa Coefficient~~
2016	0.9274~~0.96~~	0.8854~~0.95~~	0.8632~~0.95~~	0.8741~~0.95~~	0.9769~~0.93~~
2017	0.9249~~0.99~~	0.8797~~0.96~~	0.8744~~0.97~~	0.8770~~0.96~~	0.9746~~0.95~~
2018	0.9138~~0.98~~	0.9311~~0.96~~	0.8538~~0.97~~	0.8908~~0.96~~	0.9710~~0.94~~
2019	0.9355~~0.96~~	0.9040~~0.95~~	0.9033~~0.95~~	0.9036~~0.95~~	0.9804~~0.94~~
2020	0.9249~~0.93~~	0.8797~~0.95~~	0.8744~~0.94~~	0.8770~~0.94~~	0.9746~~0.92~~
2021	0.9409~~0.97~~	0.9437~~0.93~~	0.9183~~0.95~~	0.9308~~0.95~~	0.9846~~0.93~~
2022	0.9417~~0.96~~	0.9399~~0.95~~	0.9321~~0.96~~	0.9360~~0.95~~	0.9857~~0.94~~
2023	0.9450~~0.96~~	0.9455~~0.95~~	0.9400~~0.96~~	0.9427~~0.95~~	0.9871~~0.94~~
2024	0.9476	0.9346	0.9533	0.9438	0.9873

Year	AccuracyPA	PrecisionUA	RecallF1-score	F1-scoreOA	AUCKappa Coefficient
AverageMean	0.93350.96	0.91600.95	0.90140.96	0.90840.95	0.98020.94

Based on the merged data of sandy beach recognition results over 8 years, the spatial distribution of the number, length, width, and area of sandy beaches in China is shown in Fig. 5. Nationwide, a total of 2,9843347 sandy beaches were identified, with a total length of 10343.579,577.74 km, an average width of 45.1346.42 m, and a total area of approximately 260.70320.50 km²(Fig. 5).
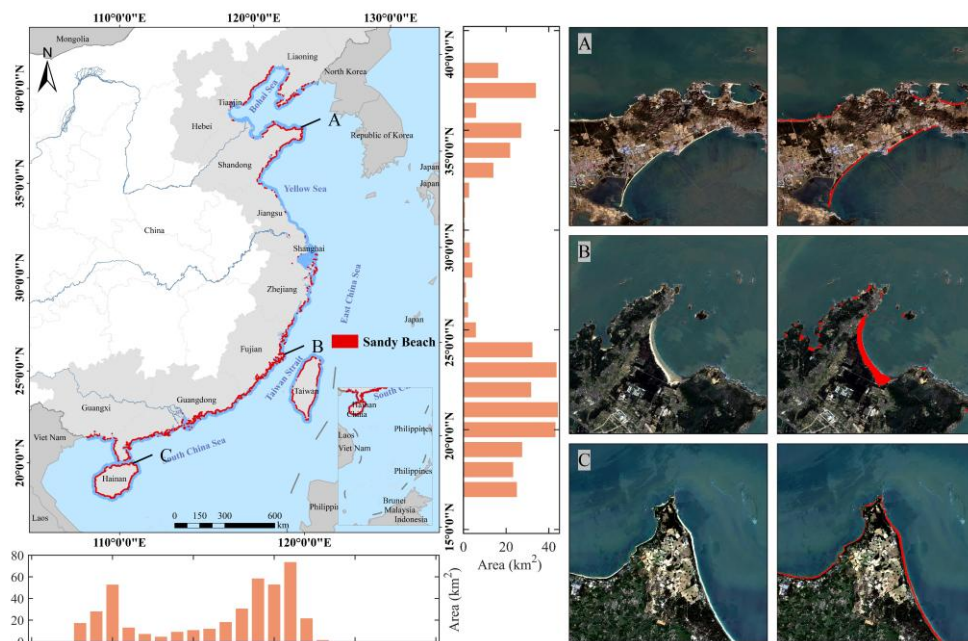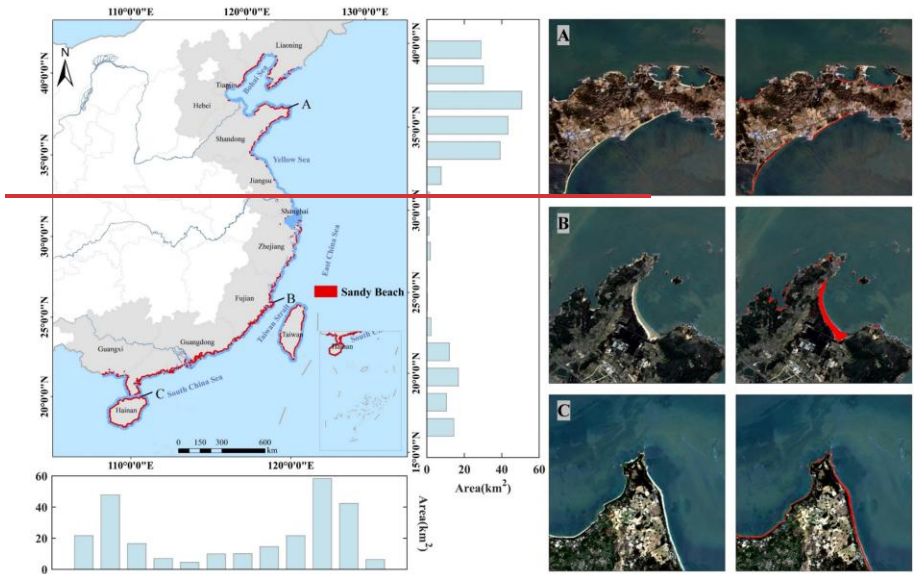
Figure 5: Distribution of sandy beaches in China and the morphology of typical coastal areas.

235   **The maps/aerial images shown are Sentinel-2 imagery obtained from the public GEE platform.**

From a provincial perspective, Guangdong has the most sandy beaches, with ~~1,080~~1096 sandy beaches, and also ranks first in both total length (~~2,794.54~~2849.39 km) and total area (~~67.83~~78.88 km²). In terms of sandy beach width, ~~Shanghai~~ Hebei has the widest sandy beaches, with an average width of ~~63.6~~68.77 m. Other regions, such as Fujian (sandy beach area ~~41.12~~54.57 km², total length ~~1,174.34~~1435.89 km, width ~~49.55~~54.91 m) and ~~Shandong~~ Hainan (sandy beach area ~~30.61~~51.65 km², total 240 length ~~1,000.66~~1977.96 km, width ~~48.32~~41.02 m), also show significant sandy beach resources. This highlights the notable spatial differences in coastal sandy beach resources across China. The results indicate that coastal sandy beach resources in China exhibit significant uneven distribution, with considerable differences in the number, shape, and scale of sandy beaches across different regions (Fig 6).

245
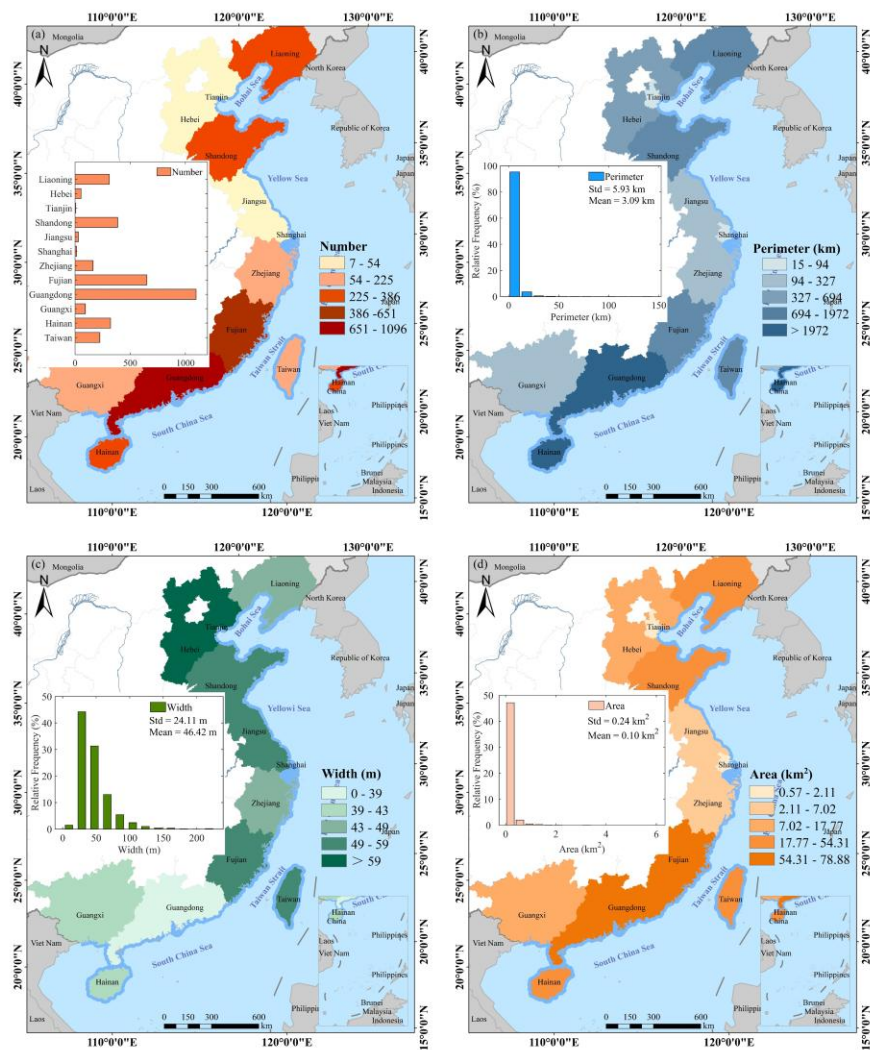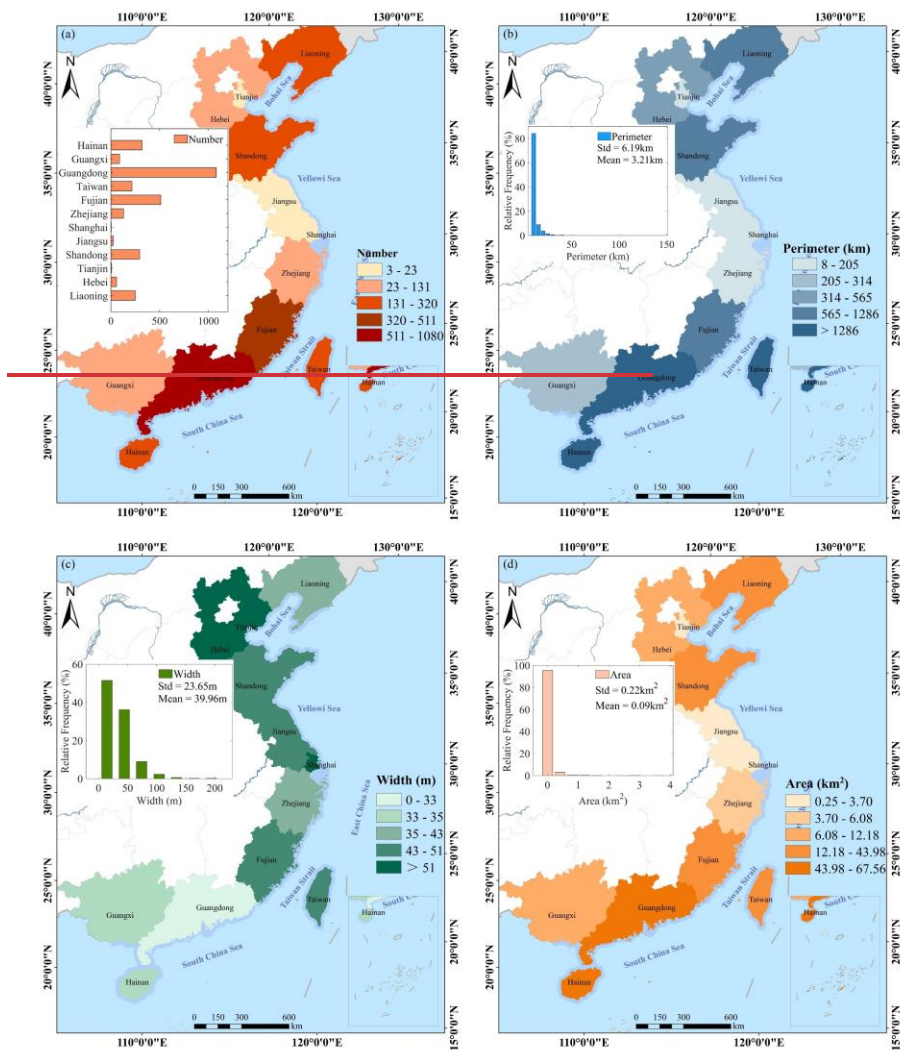
Figure 6: Spatial distribution of sandy beaches in China: (a) ~~Spatial distribution of~~ sandy beach numbers, (b) ~~Spatial distribution of~~ sandy beach length, (c) ~~Spatial distribution of~~ sandy beach width, and (d) ~~Spatial distribution of~~ sandy beach area.

设置了格式: 突出显示

4.2 Feature Importance Analysis, Model Evaluation, and Dataset Comparison~~Comparison between other datasets~~

We evaluated the variable importance of the model for the years 2016-2024 (Fig. 7). Based on the average importance ranking from 2016 to 2024, the top five features were Elevation (0.1270) > B3 (0.1242) > B2 (0.1049) > NDVI (0.0783) > VV (0.0600). When classified by feature category, the highest average importance was found in spectral features (0.3403), followed by index features (0.2458), topographic features (0.1847), texture features (0.1317), and polarization features (0.0975). The most important feature in each category was as follows: Elevation for topographic features, B3 for spectral features, NDVI for index features, VV for polarization features, and VAR for texture features.
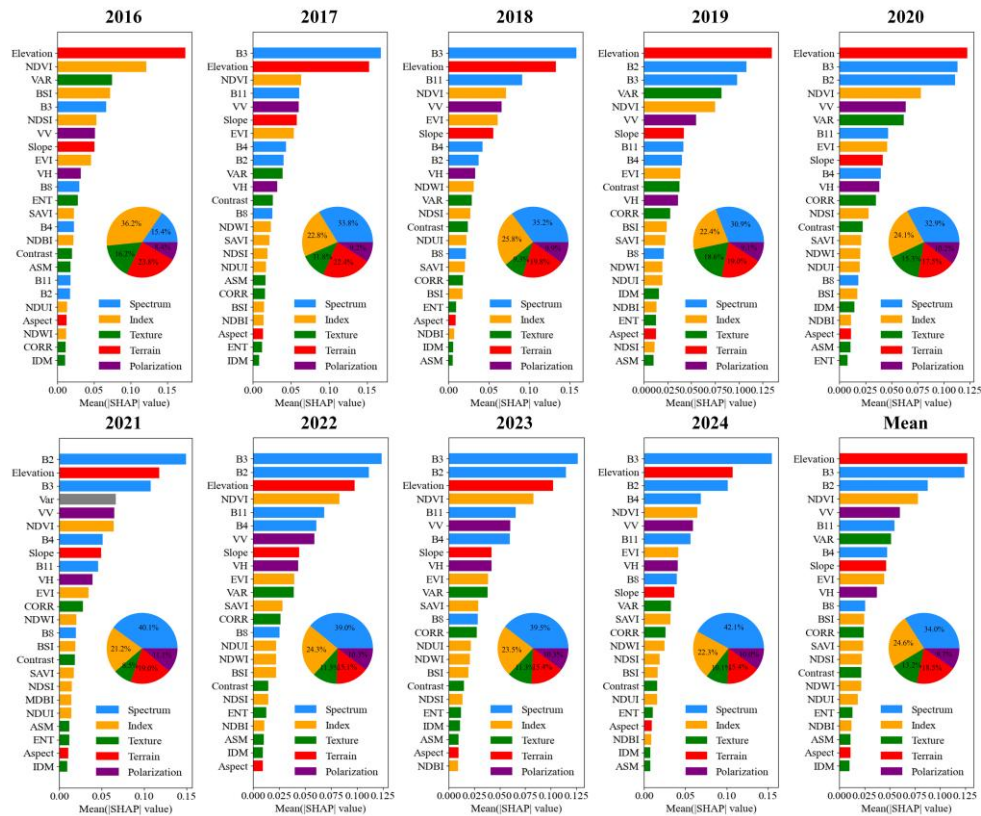
Figure 7: Analysis of model variable importance.

We evaluated the performance of our model and several other machine learning algorithms (SVM, KNN, RF, CART, and CNN) using Accuracy, Precision, Recall, F1-score, and AUC on the validation set (Table 6). Our model outperformed all others, achieving the highest accuracy (0.9335), precision (0.9160), and AUC (0.9802). It showed significantly better classification performance, especially in reducing misclassification. In comparison, the SVM model had good precision but lower recall and accuracy, while KNN performed the worst across all metrics. We evaluated the accuracy of each dataset using PA, UA, F1-score, and OA based on the validation set (Table X). To further assess the accuracy and reliability of the dataset, this study compared three published reference datasets in selected areas of Fujian, Shandong, and Guangdong (Fig. 78). Dataset 1, directly obtained from the OpenStreetMap (OSM) database generated through visual interpretation of Sentinel-2 imagery, is highly subjective and tends to misclassify non-beach areas as sandy beaches, while also missing some actual sandy beach areas. Dataset 2, constructed using a support vector machine on Sentinel-2 imagery, has high consistency with our dataset, but still misses some sandy beach areas. Dataset 3, created using an object-oriented approach, demonstrates high accuracy for other land cover types but faces significant misclassification issues with bare land and urban areas. The results show that our dataset provides higher accuracy in sandy beach classification, significantly reducing misclassification.

Table 6: The accuracy of each dataset model.

Dataset Model	Accuracy PA	Precision UA	Recall F1-score	F1-score OA	AUC
Our Dataset Model	0.9335	0.9160	0.9014	0.9084	0.9802
Dataset 1 SVM	0.8865 0.88	0.8979 0.91	0.8343 0.90	0.8636 0.89	0.9545
Dataset 2 KNN	0.7690 0.93	0.7553 0.94	0.7000 0.93	0.7249 0.93	0.8413
Dataset 3 RF	0.9183 0.85	0.9379 0.90	0.8691 0.88	0.9017 0.87	0.9752
CART	0.8802	0.8796	0.8383	0.8582	0.8750
CNN	0.8986	0.8961	0.8674	0.8809	0.9627
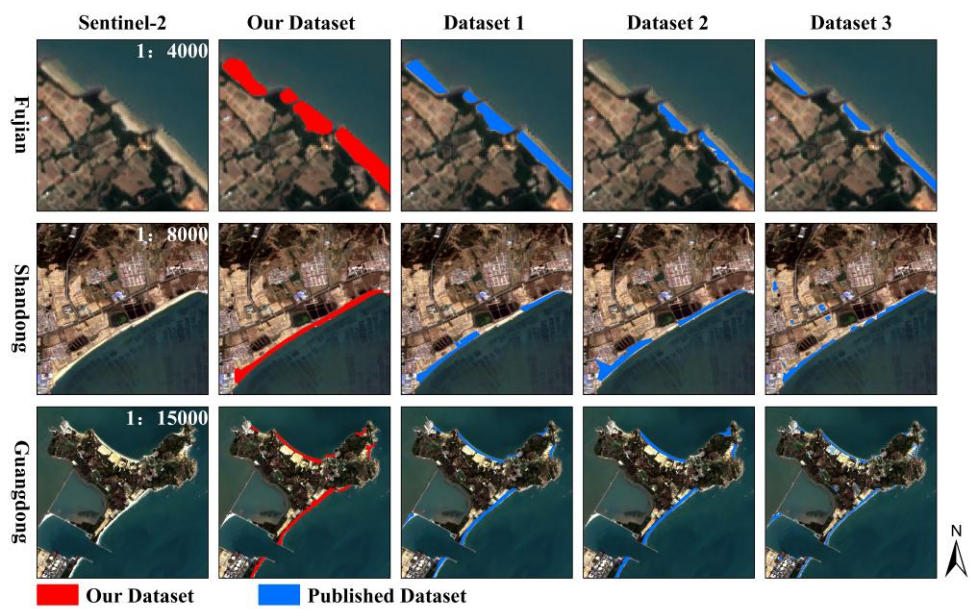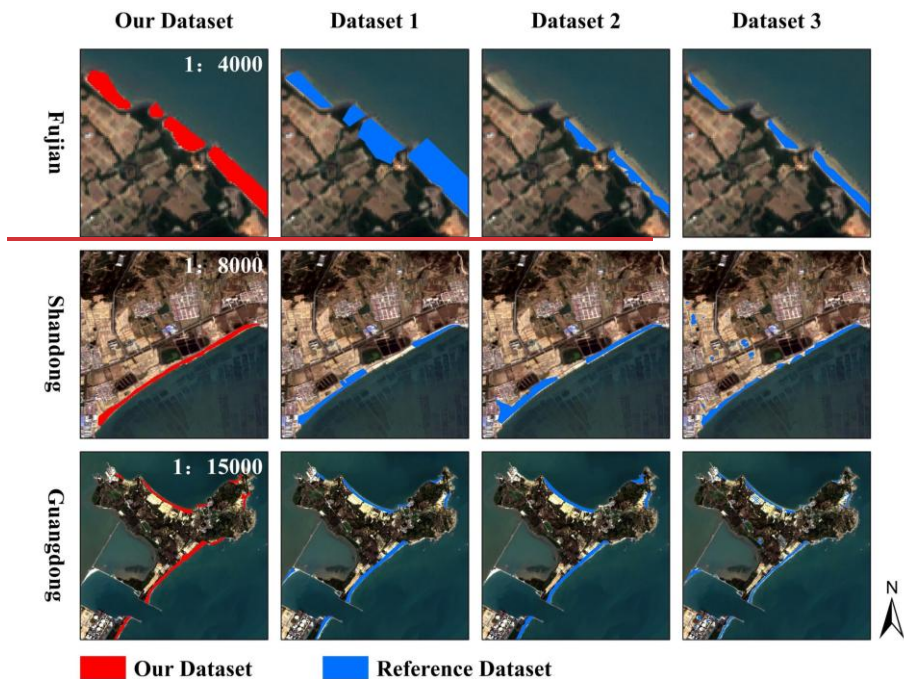
Figure ~~7~~8: Comparative analysis of sandy beaches identified in this study and three publishedreference datasets.

The maps/aerial images shown are Sentinel-2 imagery obtained from the public GEE platform.

According to the comparison results, our dataset shows significant advantages over publishedreference datasets 1, 2, and 3 in several key metrics, particularly in terms of sandy beach area, perimeter, width, and number(Fig. 9). Overall, our dataset provides a certain supplementary advantagedemonstrates a clear advantage in sandy beach area coverage, with larger areas in all regions: Fujian (54.5741.12 km²), Guangdong (78.8867.83 km²), and Taiwan (46.6040.73 km²), significantly surpassing publishedreference datasets 1 (30.352.35, 20.598.49, and 19.0724.14 km²), and 2 (29.178.49, 58.3524.14, and 25.5129.17 km²), and 3 (24.14, 28.22, and 49.35 km²). Regarding perimeter, our dataset closely matches actual sandy beach boundaries: Fujian (1435.891,174.34 km), Guangdong (2849.392,794.54 km), and Taiwan (1324.981,287.03 km), compared to publishedreference datasets 1 (581.95573.10, 826.40 and 509.22 km), and 2 (756.92334.23, 1856.62, and 906.63 km), and 3 (2,319.39 km). The excessive perimeter in reference dataset 3 is mainly due to misclassified areas. In terms of width, our dataset also outperforms publishedreference datasets 1 (52.2135.81, 20.94 and 48.42 m), and 2 (45.1842.88, 32.58 and 27.56 m), and 3 (55.22 m), with values of 54.9149.50 m in Fujian, 38.9232.83 m in Guangdong, and 57.1750.70 m in Taiwan. The

设置了格式: 突出显示
设置了格式: 突出显示
设置了格式: 突出显示
设置了格式: 突出显示
设置了格式: 突出显示
设置了格式: 突出显示
设置了格式: 突出显示
设置了格式: 突出显示
设置了格式: 突出显示
设置了格式: 突出显示
设置了格式: 突出显示
设置了格式: 突出显示
设置了格式: 突出显示
设置了格式: 突出显示
设置了格式: 突出显示
设置了格式: 突出显示
设置了格式: 突出显示
设置了格式: 突出显示
设置了格式: 突出显示
设置了格式: 突出显示
设置了格式: 突出显示
设置了格式: 突出显示
设置了格式: 突出显示
设置了格式: 突出显示
设置了格式: 突出显示
设置了格式: 突出显示
设置了格式: 突出显示

number of identified sandy beaches in our dataset is higher in published datasets, 1 and 2all regions, further highlighting the reduced misclassification and noise in our results (Fig. 89). Moreover, published datasets 3 has far higher area, perimeter, width, and number values than the other three datasets and the actual values, leading to many non-sandy beaches being incorrectly identified as sandy beaches.
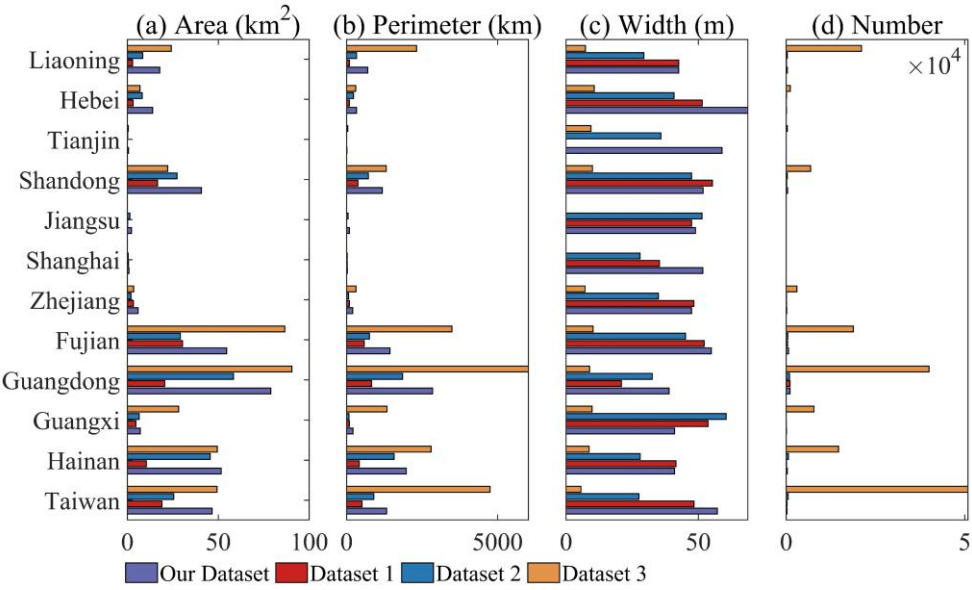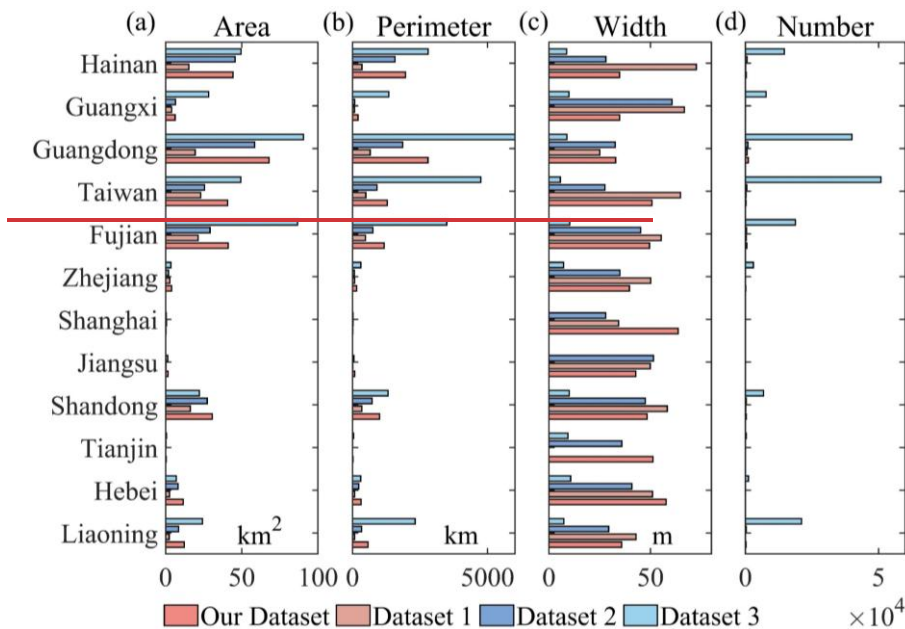
Figure 89: Provincial statistical comparison of sandy beaches in this study and three publishedreference datasets (regions sorted from south to north): (a) Length comparison, (b) Width comparison, (c) Area comparison, (d) Number comparison.

4.3 Spatial-temporal changes in human infrastructure squeeze risk

We calculated and analyzed the temporal changes in the risk areas affected by human infrastructure squeezeof human infrastructure squeeze in the study area (Fig. 910). From 1990 to 20232024, the risk area increased annually due to human infrastructure development (e.g., ports, dams, and coastal development). The area rose from 134.39109.95 km² in 1990 to 181.42245.58 km² in 20232024, a total increase of about 47.03135.63 km². The most significant increases occurred between 19901995-2000, with a nationwide increase of approximately 19.34 km² in human infrastructure squeeze risk areas during this period. However, the growth rate has slowed in recent years, with only a 3.020.80 km² increase from 2020 to 20232024, indicating stabilization due to enhanced regulation or resource saturation.
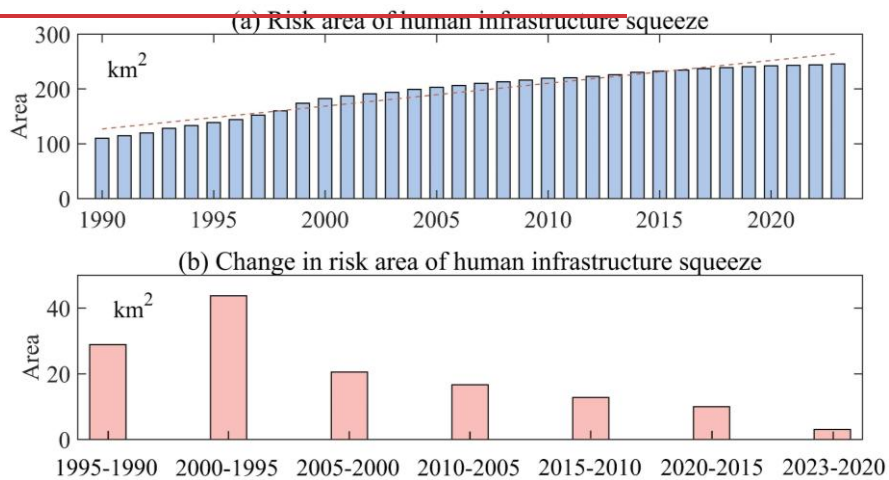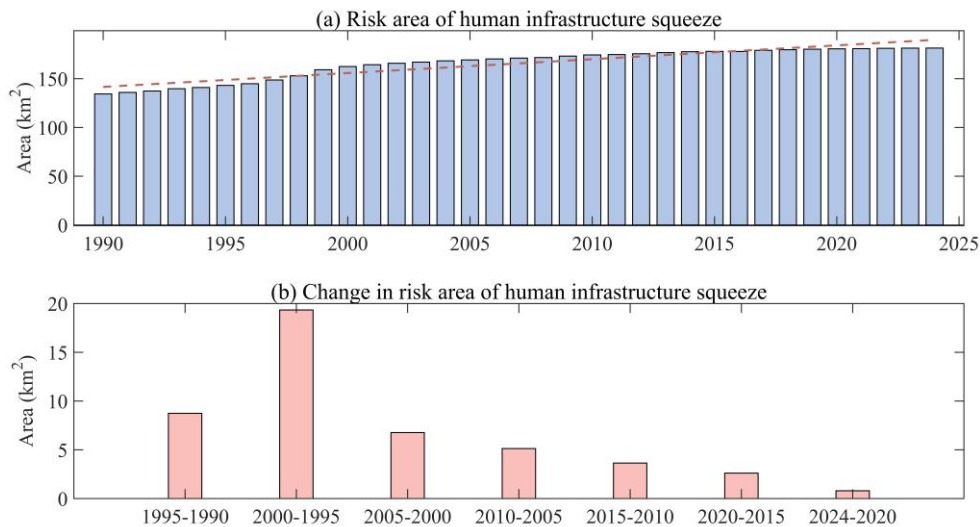
Figure 910: Interannual changes in human infrastructure squeeze on sandy beaches: (a) Risk area of human infrastructure squeeze from 1990 to 20232024, (b) Changes in risk area of human infrastructure squeeze from 1990 to 20232024.

We conducted a systematic assessment and comparative analysis of the current human infrastructure squeeze risk area in coastal regions of China in ~~2023~~2024, as well as its trend from 1990 to ~~2023~~2024 (Fig. ~~10~~11). In ~~2023~~2024, the distribution of human infrastructure squeeze risk areas showed significant regional differences. The top three regions with the largest risk

310 areas were ~~Shandong (52.97 km²), Guangdong (47.48 km²), and Taiwan (45.81 km²),~~ Guangdong (37.62 km²), Shandong (33.02 km²), Taiwan (32.52 km²), and Fujian (32.13 km²), all exceeding ~~45~~ 30 km², accounting for a significant proportion of the national coastal squeeze risk area. These regions are densely populated, economically developed, and have high coastal development density~~have high coastal development intensity~~, making them typical areas of coastal urbanization and industrial concentration. ~~Hainan~~Fujian (16.42~~33.42~~ km²) and Liaoning (~~14.18~~24.33 km²) also showed high-risk areas, reflecting ongoing interference with natural sandy beaches due to port development and coastal infrastructure. In contrast, ~~Shanghai (0.23 km²),~~

315 ~~Tianjin (0.66 km²), and Jiangsu (2.61 km²)~~ Tianjin (0.40 km²), Shanghai (0.40 km²), and Jiangsu (1.23 km²) had smaller risk areas, likely due to limited sandy beach resources. The trend analysis from 1990 to ~~2023~~2024 revealed significant growth rates in Guangdong (0.38~~1.05~~ km²/year) and Fujian (0.32~~0.73~~ km²/year), indicating rapid and substantial sandy beach squeeze risks.

设置了格式: 突出显示

320
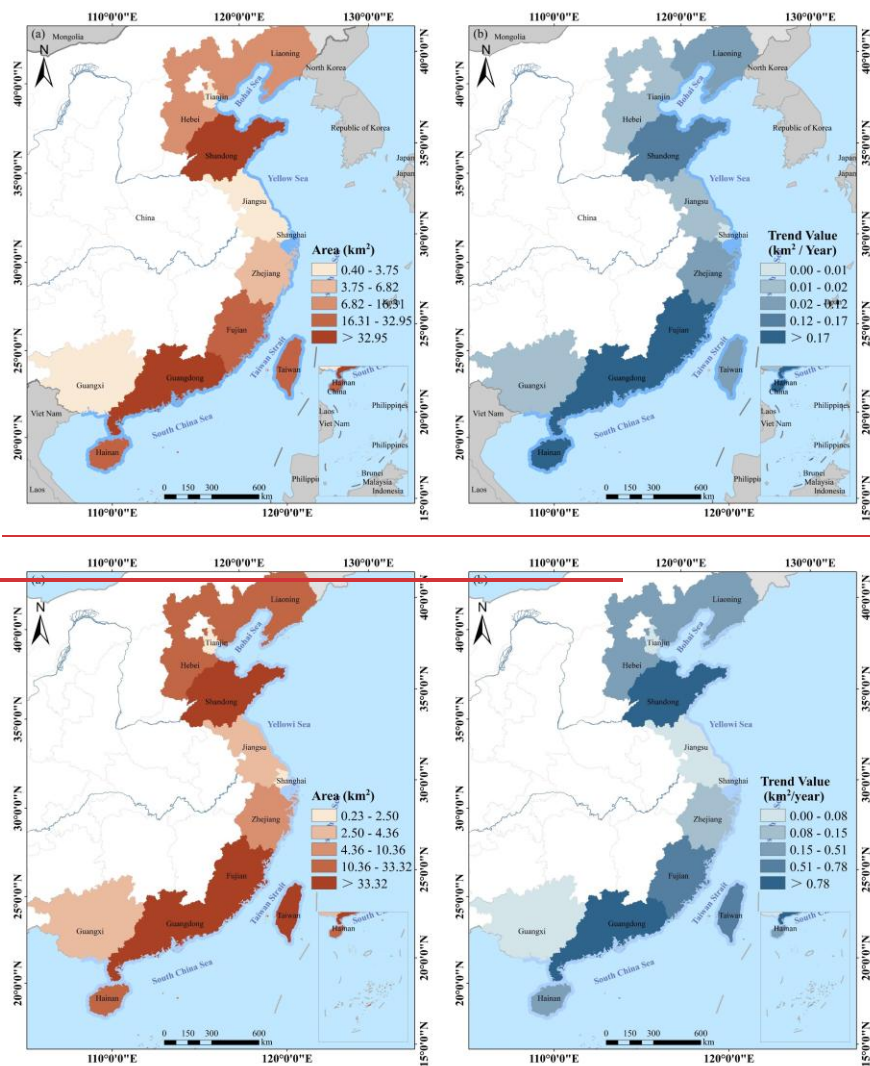
Figure ~~10~~11: Spatial changes of human infrastructure squeeze risk area: (a) ~~Current risk area of human infrastructure squeeze~~current risk area, (b) ~~Spatial changes of human infrastructure squeeze~~changes in the risk area from 1990 to ~~2023~~2024.

5 Discussion

5.1 Selection and combination of input features

325 The influence of different input features and their combinations on recognition accuracy was analyzed (Table. 7). Results show that spectral (S) ~~features~~information outperforms other single features, achieving the highest accuracy (Accuracy: 0.8976, F1-score: 0.8907). Index (I) features perform slightly worse, while terrain (T), texture (Tr), and polarization (P) features alone yield relatively low accuracies. Multi-feature fusion substantially improves model performance, with combinations involving spectral features showing the greatest gains. Among them, the "Spectral + Index + Texture + Terrain" combination achieves

330 high accuracy (Accuracy: 0.9455, F1-score: 0.9416), while the five-feature combination ("S + I + T + Tr + P") delivers the best overall results (Accuracy: 0.9476, F1-score: 0.9438, AUC: 0.9873). ~~Polarization and terrain features provide complementary information but yield moderate results. Texture features alone perform poorly. Multi-feature fusion significantly boosts performance, with the combination of "Spectral + Texture + Terrain" reaching high accuracy, and the four-feature combination achieving the best results.~~ We compared the values of sandy beach and non-sandy beach areas for

335 polarization features (VV), texture features (Correlation), and terrain features (Elevation) to explore the factors contributing to improved model accuracy (Fig. ~~11~~12). In terms of polarization features (VV), the polarization reflectance of sandy beach areas is lower, while non-sandy beach areas, such as water bodies and buildings, show higher reflectance(Novelli et al., 2016). This may be due to the different scattering characteristics of sand compared to other surfaces, such as water, which is smooth and reflects stronger signals (Lu et al., 2018). This contrast might be influenced by factors like data source and acquisition

340 angle and requires further investigation. For texture features (Correlation), sandy beach areas exhibit consistent textures due to uniform sand grain arrangements, while non-sandy beach areas show more complex textures influenced by diverse land cover (Hasituya et al., 2016). In regions with complex land cover, texture differences may diminish, affecting recognition accuracy. Regarding terrain features (Elevation), sandy beaches are typically flat and near sea level, while non-sandy beaches exhibit more significant elevation differences (Li et al., 2023). In regions with minimal terrain variation, terrain features may

345 have a weaker influence (Wang et al., 2024).

Table 7: Variations in input features and their combinations.

Input features	Accuracy~~OA~~	Precision~~UA~~	Recall~~PA~~	F1-score	AUC
S~~Spectral~~	0.8976~~0.8935~~	0.8778~~0.8806~~	0.904~~0.9141~~	0.8907~~0.8970~~	0.9603
I~~Texture~~	0.8863~~0.6433~~	0.8713~~0.6621~~	0.8845~~0.6070~~	0.8779~~0.6334~~	0.9575
T~~Polarization~~	0.7082~~0.7598~~	0.7079~~0.7391~~	0.6265~~0.8141~~	0.6647~~0.7748~~	0.7736
Tr~~Terrain~~	0.7655~~0.8270~~	0.7289~~0.7910~~	0.7836~~0.8958~~	0.7553~~0.8402~~	0.8391
P~~Spectral + Texture~~	0.7383~~0.8935~~	0.7083~~0.8827~~	0.7367~~0.9113~~	0.7222~~0.8967~~	0.8100
S + I~~Spectral + Polarization~~	0.9156~~0.8992~~	0.8994~~0.9001~~	0.9202~~0.9014~~	0.9097~~0.9008~~	0.9731
S + T~~Spectral + Terrain~~	0.9117~~0.9107~~	0.8943~~0.9001~~	0.9172~~0.9268~~	0.9057~~0.9133~~	0.9690

Input features	Accuracy~~OA~~	Precision~~UA~~	Recall~~PA~~	F1-score	AUC
S + Tr~~Texture + Polarization~~	0.9243~~0.8284~~	0.9057~~0.8246~~	0.9333~~0.8408~~	0.9193~~0.8326~~	0.9779
S + P~~Texture + Terrain~~	0.9123~~0.8435~~	0.9022~~0.8218~~	0.9085~~0.8831~~	0.9053~~0.8513~~	0.9698
I + T~~Polarization + Terrain~~	0.9076~~0.8477~~	0.8904~~0.8182~~	0.9121~~0.9000~~	0.9011~~0.8571~~	0.9681
I + Tr~~Spectral + Texture + Polarization~~	0.9194~~0.9114~~	0.9033~~0.9104~~	0.9243~~0.9155~~	0.9137~~0.9129~~	0.9758
I + P~~Spectral + Texture + Terrain~~	0.9039~~0.9271~~	0.8941~~0.9130~~	0.8982~~0.9465~~	0.8962~~0.9295~~	0.9667
T + Tr~~Spectral + Polarization + Terrain~~	0.8294~~0.9178~~	0.7943~~0.9161~~	0.8510~~0.9225~~	0.8217~~0.9193~~	0.9108
T + P~~Texture + Polarization + Terrain~~	0.8086~~0.8828~~	0.7818~~0.8750~~	0.8124~~0.8972~~	0.7968~~0.8860~~	0.8899
Tr + P~~Spectral + Texture + Polarization + Terrain~~	0.8058~~0.9321~~	0.7600~~0.9253~~	0.8469~~0.9423~~	0.8011~~0.9337~~	0.8840
S + I + T	0.9243	0.9053	0.9338	0.9193	0.9785
S + I + Tr	0.9393	0.9225	0.9481	0.9352	0.9845
S + I + P	0.9233	0.9112	0.9240	0.9176	0.9769
S + T + Tr	0.9350	0.9166	0.9453	0.9307	0.9818
S + T + P	0.9226	0.9091	0.9248	0.9169	0.9755
S + Tr + P	0.9306	0.9166	0.9348	0.9256	0.9814
I + T + Tr	0.9318	0.9129	0.9422	0.9273	0.9814
I + T + P	0.9169	0.9020	0.9201	0.9109	0.9740
I + Tr + P	0.9270	0.9102	0.9341	0.9220	0.9793
T + Tr + P	0.8597	0.8309	0.8741	0.8520	0.9350
S + I + T + Tr	0.9455	0.9309	0.9526	0.9416	0.9869
S + I + T + P	0.9295	0.9163	0.9326	0.9244	0.9808
S + I + Tr + P	0.9409	0.9266	0.9470	0.9367	0.9853
S + T + Tr + P	0.9399	0.9270	0.9442	0.9355	0.9842
I + T + Tr + P	0.9389	0.9238	0.9457	0.9346	0.9837
S + I + T + Tr + P	0.9476	0.9346	0.9533	0.9438	0.9873
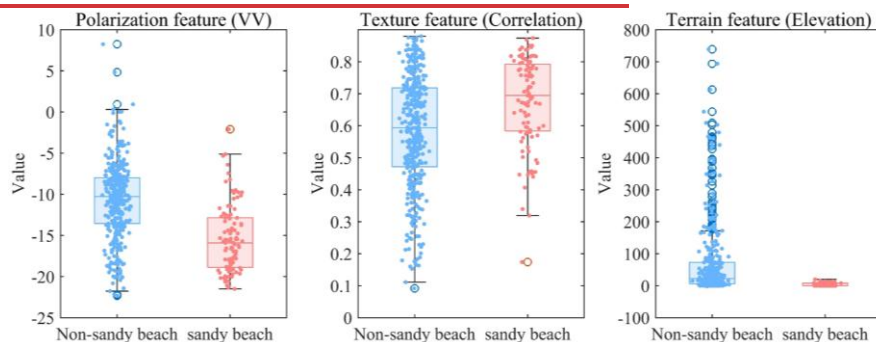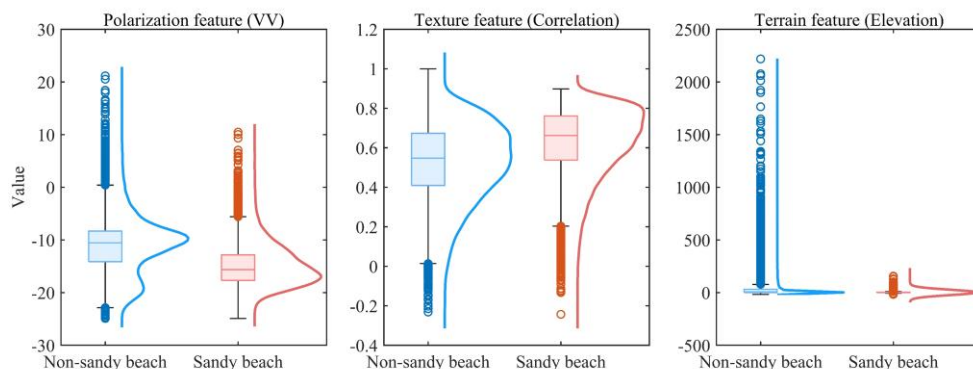
350   **Figure ~~11~~12: Comparison of polarization, texture, and terrain features between sandy beaches and non-sandy beaches.**

5.2 Effectiveness and robustness of ensemble learning

In this study, the Stacking model integrates four base classifiers—RF, ~~GBDT~~SVM, ~~XGB~~CART, and ~~LGBM~~GBDT effectively combining their strengths in feature extraction and classification. This ensemble approach enhances the model's adaptability and generalization, improving its robustness in complex sandy beach area recognition tasks (Chen et al., 2021;

355   Chrysafis et al., 2017). Each base model has its advantages: RF effectively handles high-dimensional features well and reduces overfitting, GBDT has strong nonlinear fitting capability, XGB achieves a good balance between optimization efficiency and accuracy, while LGBM performs with higher training speed and precision under large-scale and high-dimensional data conditions~~SVM performs well near class boundaries, CART is simple and efficient, while GBDT captures nonlinear relationships and feature interactions effectively~~ (Tian et al., 2025; Mugunthan et al., 2025). By integrating these models,

360 Stacking adapts better to challenges such as varying lighting, tidal conditions, and complex terrain, thus reducing misclassification. Although XGB demonstrates a slight advantage in Accuracy (0.9508), Precision (0.9433), and AUC (0.9894), and LGBM also shows certain strengths in Accuracy (0.9491), Precision (0.9414), and AUC (0.9890), the Stacking model outperforms all base learners in Recall (0.9549) and F1-score (0.9472), while exhibiting comparable performance to the base learners across the remaining metrics (Fig. 13), highlighting its robustness and reliability in overall performance. Although

365 GBDT and RF slightly outperform in the F1-score median (0.9333 and 0.9309 respectively), the Stacking model achieves comparable results (F1-score: 0.9307, OA: 0.9292) with smaller variance across experiments (Fig. 12). This demonstrates its stable performance under different data distributions. Overall, Stacking not only ensures competitive accuracy but also offers robust generalizationstrong applicability for remote sensing tasks like sandy beaches change monitoring.
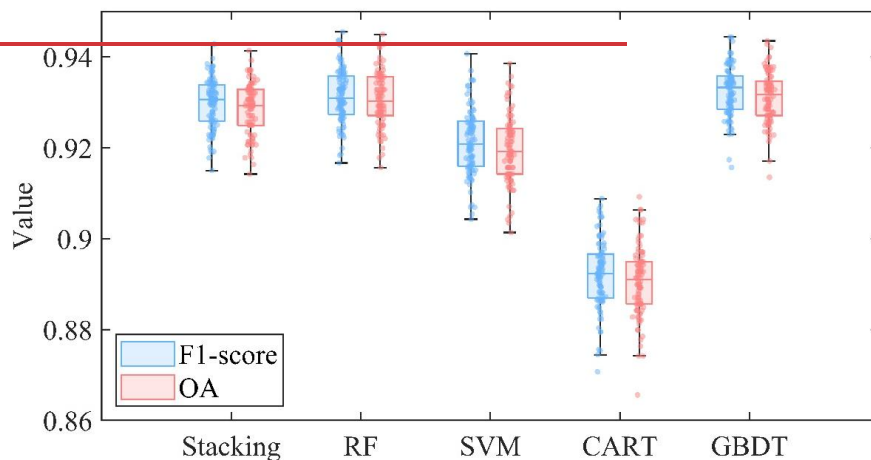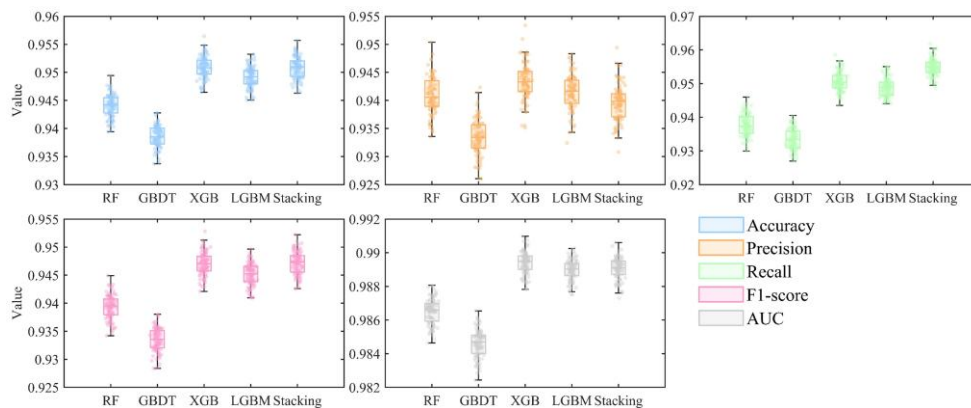
Figure 1213: Comparison of F1-score and overall accuracy across models.

5.3 Factors shaping the spatial pattern of China's sandy beaches

This study produced a 10 m resolution sandy beach dataset for China's coastal regions. The spatial distribution of sandy beaches shows a clear pattern: more in the north and the south, and fewer in the central coast. This pattern is shaped by a combination of geological structures, marine dynamics, climate conditions, and river sediment input (Tian et al., 2025; Ma et al., 2024; Wang et al., 2010). The northern coast features flat terrain and large rivers like the Yellow River and Liao River, which deliver

abundant sediment, supporting sandy beach formation (Zhang et al., 2022). In the south, strong marine forces and tropical climates allow rivers to carry large amounts of sediment to the coast, where wide sandy beaches form under suitable conditions (Zhou et al., 2023; Mentaschi et al., 2018). In contrast, the central coast is dominated by bedrock and muddy coastlines. Major rivers such as the Yangtze mainly contribute to tidal flats and muddy shores rather than typical sandy beaches (Kuai et al., 2021; Liu et al., 2020). Overall, the distribution of sandy beaches in China is shaped by sediment supply, coastal type, and hydrodynamic conditions, with more beaches in the north and south, and fewer along the central coast. Overall, the distribution of sandy beaches in China reflects the combined effects of sediment supply, coastal type, and hydrodynamic conditions, resulting in more sandy beaches in the north and south, and fewer on the central coast.

5.4 Exploration of the factors affecting the change in human infrastructure squeeze risk area

Based on the 1990-2023 2024 Sen's slope trend analysis, several patterns emerge when analyzing the relationship between human infrastructure squeeze risk areas and related factors across regions (Fig. 13 14). Economically developed regions like Shanghai, Jiangsu, and Tianjin show slower growth in squeeze risk areas. This can be attributed to their smaller sandy beach areas, which limit the available space for human activities, and their higher per capita GDP, which is associated with more efficient urban planning and infrastructure development, leading to slower increases in squeeze risk. In contrast, regions with larger sandy beach areas, such as Guangdong, Shandong, Fujian, Taiwan, and Hainan, show faster growth in squeeze risk, as more space for development leads to higher risk over time. Additionally, regions with larger resident population, like Guangdong, Shandong, and Hebei, experience a positive correlation between population growth and squeeze risk. As the resident population increases, urbanization accelerates, putting more pressure on infrastructure and increasing the squeeze risk. Both built-up area and road area are positively correlated with squeeze risk, as their expansion reflects urban growth, intensifying competition for space.
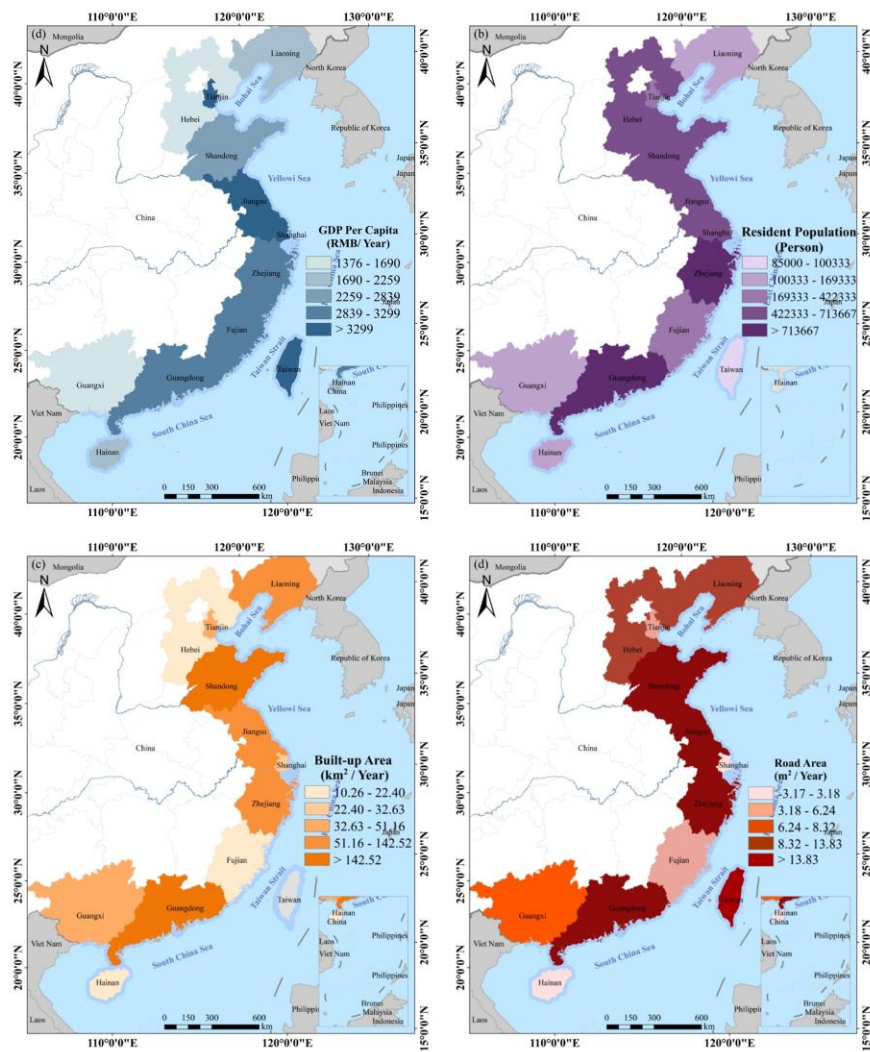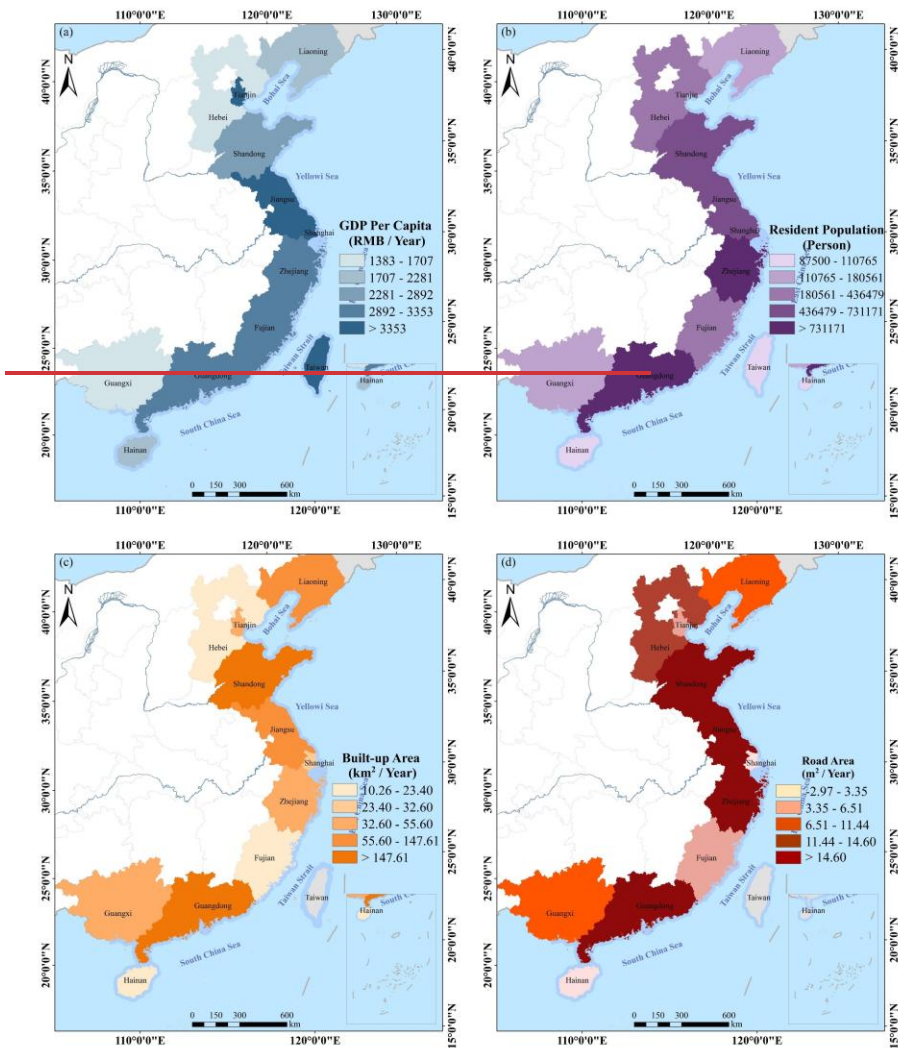
Figure ~~13~~14: Spatial changes of various factors from 1990 to ~~2023~~2024: (a) ~~per capita GDP change~~Spatial change of per capita GDP, **(b)** ~~resident population change~~Spatial change of resident population, **(c)** ~~built-up area change~~Spatial change of built-up area, **(d)** ~~road area change~~Spatial change of road area.

400

We conducted a comprehensive analysis of the 1990, 2000, 2010, and 2020 data for the typical areas of human infrastructure squeeze risk in Jinjiang District, Quanzhou District, and Fengze District of Quanzhou, as detailed in the appendix. The analysis focused on the changes in indicators such as GDP, population density, built-up area, and road length. The results show that all these indicators have significantly increased over the past few decades, which is closely related to the risk of human infrastructure squeeze on sandy beaches. Specifically, with the growth of GDP, the expansion of economic activities has led to a continuous concentration of population in these areas, increasing the potential pressure on sandy beaches and the surrounding ecosystem. The expansion of built-up areas reflects the progress of urbanization, which, especially in vulnerable ecological regions such as sandy beaches, is often accompanied by a squeeze on natural resources. Although the increase in road length has promoted economic development, it has also intensified the risk of the squeeze on coastlines and surrounding sandy beaches.

5.5 Limitations of the proposed method and dataset

This study combines stacking ensemble learning models with remote sensing imagery to create a 10m resolution sandy beach dataset, integrating multi-dimensional features such as spectral, terrain, polarization, and texture features. However, the study has some areas for improvement: (1) The sandy beach area is significantly affected by tidal changes, and the remote sensing images acquired at different tidal levels may exhibit considerable spatial differences. The current study has not fully addressed the issue of tidal phase matching. Future research should combine tidal prediction models or measured tidal data to select multi-temporal remote sensing images that are consistent with the target tidal phase, reducing the impact of tidal variations on beach extraction and improving the spatiotemporal accuracy of beach extraction. (2) This study has preliminarily applied the Stacking ensemble learning method; however, there is still room for optimization in model selection, fusion strategy, and feature contribution evaluation. Future research can further optimize the base model structure, explore the synergistic effects between different models, and incorporate feature importance analysis to enhance the stability and classification accuracy of the ensemble model. (3) Currently, the assessment of human infrastructure squeeze risk in this study primarily relies on impervious surface expansion and buffer zone analysis. However, with relatively low spatial and temporal resolution, it is difficult to accurately depict the dynamic process of human infrastructure squeeze on sandy beaches. Future research should introduce higher spatial and temporal resolution data (e.g., high-frequency remote sensing monitoring, annual building change data, etc.) to enable continuous dynamic monitoring and analysis of the human infrastructure squeeze process.

6 Data availability

The dataset on the distribution of sandy beaches in China and the distribution of human infrastructure squeeze risk is available at: https://doi.org/10.5281/zenodo.15307240 (Meng et al., 2025).

7 Conclusions

This study used ensemble learning algorithms to identify sandy beach areas between 2016 and 2023 2024 and validated the superiority of the method through various classification metrics. The results demonstrate that the method exhibits high stability and accuracy in the beach classification task, effectively distinguishing sandy beaches from other land types. Additionally, there are significant regional differences, with some regions having abundant sandy beach resources while others have relatively fewer sandy beach areas, indicating an uneven distribution of resources. By comparing with several publishedreference datasets, the proposed dataset in this study showed higher accuracy and reliability, especially in some typical coastal areas, ensuring precise classification of sandy beach regions. This provides more accurate data support for sandy beach resource management and ecological protection, particularly in the context of increasingly scarce beach resources.

In addition to identifying sandy beach resources, this study also focused on the risk of infrastructure squeeze on sandy beach resources along China's coast. The study found that as infrastructure projects such as port construction and seawall building continue to advance, coastal areas are facing the gradual squeeze of their sandy beaches. Although the rate of expansion in some regions has slowed, the pressure from infrastructure development on beach resources continues to persist. The impact of infrastructure squeeze varies between regions, with some regions facing more severe challenges, while others experience relatively minor changes in sandy beach resources. These findings provide important theoretical support for future sandy beach resource management and protection, highlighting the balance between infrastructure development and ecological preservation. This is particularly important in the context of rapid urbanization and economic development. Achieving sustainable sandy beach resource protection will be a crucial focus for future coastal region policy planning.

References

Bai, Z., Ye, Y., Zhou, L., Li, Z., and Yin, G.: Robust registration of aerial images and LiDAR data using spatial constraints and Gabor structural features, ISPRS J. Photogramm. Remote Sens., 181, 129–147, 2021. https://doi.org/10.1016/j.isprsjprs.2021.09.010

Bao, Z., Sha, J., Li, X., Hanchiso, T., and Shifaw, E.: Monitoring of beach litter by automatic interpretation of unmanned aerial vehicle images using the segmentation threshold method, Mar. Pollut. Bull., 137, 388–398, doi:10.1016/j.marpolbul.2018.08.009, 2018.

Barbier, E. B., Hacker, S. D., Kennedy, C., Koch, E. W., Stier, A. C., and Silliman, B. R.: The value of estuarine and coastal ecosystem services, Ecol. Monogr., 81(2), 169–193, doi:10.1890/10-1510.1, 2011.

Baum-Snow, N., Brandt, L., Henderson, J. V., Turner, M. A., and Zhang, Q.: Roads, Railroads, and Decentralization of Chinese Cities, Rev. Econ. Stat., 99(3), 435–448, doi:10.1162/REST_a_00643, 2017.

Blenkinsopp, C.E., Bayle, P.M., Conley, D.C., Masselink, G., Gulson, E., Kelly, I., Almar, R., Turner, I.L., Baldock, T.E., Beuzen, T., McCall, R.T., Rijper, H., Reniers, A., Troch, P., Gallach-Sanchez, D., Hunter, A.J., Bryan, O., Hennessey, G.,

Ganderton, P., Tissier, M., Kudella, M., and Schimmels, S.: High-resolution, large-scale laboratory measurements of a sandy beach and dynamic cobble berm revetment, Sci. Data, 8, 22, 2021. https://doi.org/10.1038/s41597-021-00805-1.

Brščić, K., and Šugar, T.: Users' perceptions and satisfaction as indicators for sustainable beach management, Tour. Hosp.
465   Manag., 26(1), 33–48, doi:10.1016/j.ocecoaman.2009.02.001, 2020.

Cao, B., Yu, L., Naipal, V., Ciais, P., Li, W., Zhao, Y., Wei, W., Chen, D., Liu, Z., and Gong, P.: A 30 m terrace mapping in China using Landsat 8 imagery and digital elevation model based on the Google Earth Engine, Earth Syst. Sci. Data, 13(5), 2437–2456, doi:10.5194/essd-13-2437-2021, 2021.

Chen, B., Tu, Y., Song, Y., Theobald, D. M., Zhang, T., Ren, Z., Li, X., Yang, J., Wang, J., Wang, X., Gong, P., Bai, Y., and
470   Xu, B.: Mapping essential urban land use categories with open big data: Results for five metropolitan areas in the United States of America, ISPRS J. Photogramm. Remote Sens., 178, 203–218, doi:10.1016/j.isprsjprs.2021.06.010, 2021.

Chen, C., Liang, J., Xie, F., Hu, Z., Sun, W., Yang, G., Yu, J., Chen, L., Wang, L., Wang L., Chen, H., He, X., and Zhang, Z.: Temporal and spatial variation of coastline using remote sensing images for Zhoushan archipelago, China, Int. J. Appl. Earth Obs. Geoinf., 107, doi:10.1016/j.jag.2022.102711, 2022.

475   Chen, Y., Xu, C., Ge, Y., Zhang, X., and Zhou, Y.: A 100 m gridded population dataset of China's seventh census using ensemble learning and big geospatial data, Earth Syst. Sci. Data, 16(8), 3705–3718, doi:10.5194/essd-16-3705-2024, 2024.

Chrysafis, I., Mallinis, G., Gitas, I., and Tsakiri-Strati, M.: Estimating Mediterranean forest parameters using multi seasonal Landsat 8 OLI imagery and an ensemble learning method, Remote Sens. Environ., 199, 154–166, doi:10.1016/j.rse.2017.07.018, 2017.

480   Duan, Y., Tian, B., Li, X., Liu, D., Sengupta, D., Wang, Y., and Peng, Y.: Tracking changes in aquaculture ponds on the China coast using 30 years of Landsat images, Int. J. Appl. Earth Obs. Geoinf., 102, doi:10.1016/j.jag.2021.102383, 2021.

Feng, J., Kong, L., Li, H., Cannon, N., Chang, X., and Ma, L.: Evaluation of the sustainable development capacity of bay cities in China in the context of Blue Bay Remediation Action, Sustainability, 17(7), doi:10.3390/su17074567, 2025.

Hasituya, Chen, Z., Wang, L., Wu, W., Jiang, Z., and Li, H.: Monitoring plastic-mulched farmland by Landsat-8 OLI imagery
485   using spectral and textural features, Remote Sens., 8(4), doi:10.3390/rs8040297, 2016.

Jia, M., Wang, Z., Mao, D., Ren, C., Wang, C., and Wang, Y.: Rapid, robust, and automated mapping of tidal flats in China using time series Sentinel-2 images and Google Earth Engine, Remote Sens. Environ., 255, 112320, doi:10.1016/j.rse.2021.112320, 2021.

Jiang, W., Tian, B., Duan, Y., Chen, C., and Hu, Y.: Rapid mapping and spatial analysis on the distribution of photovoltaic
490   power stations with Sentinel-1&2 images in Chinese coastal provinces, Int. J. Appl. Earth Obs. Geoinf., 118, 103206, doi:10.1016/j.jag.2023.103206, 2023.

Kuai, Y., Tao, J., Zhou, Z., Aarninkhof, S., and Wang, Z. B.: Sediment characteristics and intertidal beach slopes along the Jiangsu coast, China, J. Mar. Sci. Eng., 9(3), 273, doi:10.3390/jmse9030273, 2021.

Lansu, E. M., Reijers, V. C., Hofer, S., Luijendijk, A., Rietkerk, M., Wassen, M. J., Lammerts, E. J., and van der Heide.: A global analysis of how human infrastructure squeezes sandy coasts, Nat. Commun., 15(1), 432, doi:10.1038/s41467-023-44120-5, 2024.

Latella, M., Luijendijk, A., Moreno-Rodenas, A. M., and Camporeale, C.: Satellite image processing for the coarse-scale investigation of sandy coastal areas, Remote Sens., 13(22), 4552, doi:10.3390/rs13224552, 2021.

Li, J., Wang, H., Wang, J., Zhang, J., Lan, Y., and Deng, Y.: Combining multi-source data and feature optimization for plastic-covered greenhouse extraction and mapping using the Google Earth Engine: A case in Central Yunnan Province, China, Remote Sens., 15(13), 3356, doi:10.3390/rs15133356, 2023.

Li, Y., and Niu, Z.: Systematic method for mapping fine-resolution water cover types in China based on time series Sentinel-1 and 2 images, Int. J. Appl. Earth Obs. Geoinf., 106, 102670, doi:10.1016/j.jag.2021.102670, 2022.

Liao, L., and Zhu, X.: Predicting wildfire risk in southwestern Saudi Arabia using machine learning and geospatial analysis, Remote Sens., 17, 3516, doi:10.3390/rs17213516, 2025.

Lin, J., Jin, X., Ren, J., Liu, J., Liang, X., and Zhou, Y.: Rapid mapping of large-scale greenhouse based on integrated learning algorithm and Google Earth Engine, Remote Sens., 13(7), 1337, doi:10.3390/rs13071337, 2021.

Liu, G., Cai, F., Qi, H., Liu, J., Lei, G., Zhu, J., Cao, H., Zheng, J., Zhao, S., and Yu, F.: A summary of beach nourishment in China: The past decade of practices, Shore Beach, 88(1), 65–73, doi:10.34237/1008836, 2020.

Lu, L., Tao, Y., and Di, L.: Object-based plastic-mulched landcover extraction using integrated Sentinel-1 and Sentinel-2 data, Remote Sens., 10(11), 1723, doi:10.3390/rs10111723, 2018.

Lu, Y., Yuan, J., Lu, X., Su, C., Zhang, Y., Wang, C., Cao, X., Li, Q., Su, J., Ittekkot, V., Garbutt, R. A., Bush, S., Fletcher, S., Wagey, T., Kachur, A., and Sweijd, N.: Major threats of pollution and climate change to global coastal ecosystems and enhanced management for sustainability, Environ. Pollut., 239, 670–680, doi:10.1016/j.envpol.2018.04.135, 2018.

Ma, F., Lü, P., Cao, M., Yu, J., and Xia, Z.: Morphological and sedimentary characteristics of raked linear dunes in the southeastern Taklimakan Desert, China, Aeolian Res., 67–69, doi:10.1016/j.aeolia.2024.100923, 2024.

Masria, A.: Bridging coastal challenges: The role of remote sensing and future research, Reg. Stud. Mar. Sci., 73, doi:10.1016/j.rsma.2024.103502, 2024.

Mattson, M., Sousa, D., Quandt, A., Ganster, P., and Biggs, T.: Mapping multi-decadal wetland loss: Comparative analysis of linear and nonlinear spatiotemporal characterization, Remote Sens. Environ., 302, doi:10.1016/j.rse.2023.113969, 2024.

Mejjad, N., Rossi, A., and Pavel, A. B.: The coastal tourism industry in the Mediterranean: A critical review of the socio-economic and environmental pressures & impacts, Tour. Manag. Perspect., 44, doi:10.1016/j.tmp.2022.101007, 2022.

Meng, J., Xu, D. Y., Tao, Z. X., and Ge, Q. S.: Spatial Patterns of Sandy Beaches in China and Risk Analysis of Human Infrastructure Squeeze Based on Multi-Source Data and Ensemble Learning, Zenodo [data set], doi:10.5281/zenodo.15307240, 2025.

Mentaschi, L., Vousdoukas, M. I., Pekel, J. F., Voukouvalas, E., and Feyen, L.: Global long-term observations of coastal erosion and accretion, Sci. Rep., 8, 12876, doi:10.1038/s41598-018-30904-w, 2018.

Miao, L., Chen, B., Webster, C., Gong, P., and Xu, B.: The land-sea interface mapping: China's coastal land covers at 10 m for 2020, Sci. Bull., 67(17), 1750–1754, 2022.

530 Mugunthan, J. S., Duguay, C. R., and Zakharova, E.: Machine learning based classification of lake ice and open water from Sentinel-3 SAR altimetry waveforms, Remote Sens. Environ., 299, doi:10.1016/j.rse.2023.113891, 2023.

Nativí-Merchán, S., Caiza-Quinga, R., Saltos-Andrade, I., Martillo-Bustamante, C., Andrade-García, G., Quiñonez, M., Cervantes, E., and Cedeño, J..: Coastal erosion assessment using remote sensing and computational numerical model. Case of study: Libertador Bolivar, Ecuador, Ocean Coast. Manag., 214, doi:10.1016/j.ocecoaman.2021.105894. 2021.

535 Nemmaoui, A., Aguilar, M. A., Aguilar, F. J., Novelli, A., and García Lorca, A.: Greenhouse crop identification from multi-temporal multi-sensor satellite imagery using object-based approach: A case study from Almería (Spain), Remote Sens., 10(11), doi:10.3390/rs10111751, 2018.

Ni, M., Xu, N., Ou, Y., Yao, J., Li, Z., Mo, F., Huang, C., Xin, H., and Xu, H.: The first 10-m China's national-scale sandy beach map in 2022 derived from Sentinel-2 imagery, Int. J. Digit. Earth, 17(1), doi:10.1080/17538947.2024.2425163, 2024.

540 Novelli, A., Aguilar, M. A., Nemmaoui, A., Aguilar, F. J., and Tarantino, E.: Performance evaluation of object based greenhouse detection from Sentinel-2 MSI and Landsat 8 OLI data: A case study from Almería (Spain), Int. J. Appl. Earth Obs. Geoinf., 52, 403–411, doi:10.1016/j.jag.2016.07.011, 2016.

Pan, X., Yang, F., Gao, L., Chen, Z., Zhang, B., Fan, H., and Ren, J.: Building extraction from high-resolution aerial imagery using a generative adversarial network with spatial and channel attention mechanisms, Remote Sens., 11, 917, 545 doi:10.3390/rs11080917, 2019.

Pesaresi, M. and Politis, P.: GHS-BUILT-H R2023A – GHS Building Height, Derived from AW3D30, SRTM30, and Sentinel-2 Composite (2018), Eur. Comm., Joint Res. Cent., 2023, doi:10.2905/85005901-3A49-48DD-9D19-6261354F56FE.

Pickens, A. H., Hansen, M. C., Hancher, M., Stehman, S. V., Tyukavina, A., Potapov, P., Marroquin, B., and Sherani, Z.: Mapping and sampling to characterize global inland water dynamics from 1999 to 2018 with full Landsat time-series, Remote 550 Sens. Environ., 243, doi:10.1016/j.rse.2020.111792, 2020.

Ponte Lira, C., Nobre Silva, A., Taborda, R., and Freire de Andrade, C.: Coastline evolution of Portuguese low-lying sandy coast in the last 50 years: an integrated approach, Earth Syst. Sci. Data, 8(1), 265–278, doi:10.5194/essd-8-265-2016, 2016.

Qiao, L., and Xia, H.: The impact of drought time scales and characteristics on gross primary productivity in China from 2001 to 2020, Geo-spat. Inf. Sci., 28, 284–302, doi:10.1080/10095020.2023.2223554, 2024.

555 Rabehi, W., Amin Larabi, M. E., Benabbou, O., Kreri, S., and Dellani, H.: Sandy beach mapping using a deep learning approach: potential method for automated monitoring of Algerian coastal erosion, J. Coast. Res., 39, 960–970, doi:10.2112/JCOASTRES-D-22-00050.1, 2023.

Ranasinghe, R.: Assessing climate change impacts on open sandy coasts: a review, Earth-Sci. Rev., 160, 320–332, doi:10.1016/j.earscirev.2016.07.011, 2016.

设置了格式: 字体: (中文) Times New Roman, 突出显示

Rhyma, P. P., Norizah, K., Hamdan, O., Faridah-Hanum, I., and Zulfa, A. W.: Integration of normalized difference vegetation index and soil-adjusted vegetation index for mangrove vegetation delineation, Remote Sens. Appl. Soc. Environ., 17, 100276, doi:10.1016/j.rsase.2020.100276, 2020.

Rodríguez-Padilla, I., Mariño-Tapia, I., and Ruiz de Alegría-Arzaburu, A.: Daily timescale analysis of sediment transport and terrain changes on a mesotidal sandy beach under low to moderate wave conditions, Mar. Geol., 474, 107597, doi:10.1016/j.margeo.2024.107597, 2024.

Roy, P. S., Sharma, K. P., and Jain, A.: Stratification of density in dry deciduous forest using satellite remote sensing digital data—an approach based on spectral indices, J. Biosci., 21, 723–734, doi:10.1007/BF02703124, 1996.

Salameh, E., Frappart, F., Almar, R., Baptista, P., Heygster, G., Lubac, B., Raucoules, D., Almeida, L. P., Bergsma, E. W. J., Capo, S., De Michele, M., Idier, D., Li, Z., Marieu, V., Poupardin, A., De Silva, P. A., Turki, I., and Laignel, B.: Monitoring beach topography and nearshore bathymetry using spaceborne remote sensing: a review, Remote Sens., 11, 2212, doi:10.3390/rs11192212, 2019.

Sekar, C. S., Kankara, R. S., and Kalaivanan, P.: Pixel-based classification techniques for automated shoreline classification on open sandy coast using different optical satellite images, Arab. J. Geosci., 15, 978, doi:10.1007/s12517-022-10014-1, 2022.

Sekovski, I., Stecchi, F., Mancini, F., and Del Rio, L.: Image classification methods applied to shoreline classification on very high-resolution multispectral imagery, Int. J. Remote Sens., 35, 3556–3578, doi:10.1080/01431161.2014.903436, 2014.

Splinter, K. D., Harley, M. D., and Turner, I. L.: Remote sensing is changing our view of the coast: insights from 40 years of monitoring at Narrabeen-Collaroy, Australia, Remote Sens., 10, 1744, doi:10.3390/rs10111744, 2018.

Sun, S., Xue, Q., Xing, X., Zhao, H., and Zhang, F.: Remote sensing image interpretation for coastal zones: a review, Remote Sens., 16, 4016, doi:10.3390/rs16244016, 2024.

Tassi, A., and Vizzari, M.: Object-oriented LULC classification in Google Earth Engine combining SNIC, GLCM, and machine learning algorithms, Remote Sens., 12, 3771, doi:10.3390/rs12223771, 2020.

Temmerman, S., Meire, P., Bouma, T. J., Herman, P. M., Ysebaert, T., and De Vriend, H. J.: Ecosystem-based coastal defence in the face of global change, Nature, 504, 79–83, doi:10.1038/nature12859, 2013.

Tian, B., Wu, W., Yang, Z., and Zhou, Y.: Drivers, trends, and potential impacts of long-term coastal reclamation in China from 1985 to 2010, Estuar. Coast. Shelf Sci., 170, 83–90, doi:10.1016/j.ecss.2016.01.006, 2016.

Tian, P., Liu, Y., Li, J., Pu, R., Cao, L., Zhang, H., Ai, SS., and Yang, Y.: Mapping coastal aquaculture ponds of China using Sentinel SAR images in 2020 and Google Earth Engine, Remote Sens., 14, 5473, doi:10.3390/rs14215473, 2022.

Tian, S., Sha, A., Luo, Y., Ke, Y., Spencer, R., Hu, X., Ning, M., Zhao, Y., Deng, R., Gao, Y., Liu, Y., and Li, D.: A novel framework for river organic carbon retrieval through satellite data and machine learning, ISPRS J. Photogramm. Remote Sens., 221, 109–123, doi:10.1016/j.isprsjprs.2025.01.002, 2025.

Tian, W., Dong, Y., Fu, S., Zhang, S., Huang, D., and Yang, L.: Surfzone–beach–dune interactions on the Chinese coasts, Mar. Geol., 481, 107637, doi:10.1016/j.margeo.2025.107637, 2025.

Toure, S., Diop, O., Kpalma, K., and Maiga, A. S.: Shoreline detection using optical remote sensing: a review, ISPRS Int. J. Geo-Inf., 8, 77, doi:10.3390/ijgi8020077, 2019.

595 Turner, I. L., Harley, M. D., Short, A. D., Simmons, J. A., Bracs, M. A., Phillips, M. S., and Splinter, K. D.: A multi-decade dataset of monthly beach profile surveys and inshore wave forcing at Narrabeen, Australia, Sci. Data, 3, 160024, doi:10.1038/sdata.2016.24, 2016.

Valderrama-Landeros, L., Flores-Verdugo, F., and Flores-de-Santiago, F.: Assessing the coastal vulnerability by combining field surveys and the analytical potential of CoastSat in a highly impacted tourist destination, Geographies, 2, 642–656, 600 doi:10.3390/geographies2040036, 2022.

Vicens-Miquel, M., Medrano, F. A., Tissot, P. E., Kamangir, H., Starek, M. J., and Colburn, K.: A deep learning based method to delineate the wet/dry shoreline and compute its elevation using high-resolution UAS imagery, Remote Sens., 14, 6149, doi:10.3390/rs14236149, 2022.

Wang, M., Mao, D., and Xiao, X.: Interannual changes of coastal aquaculture ponds in China at 10-m spatial resolution during 605 2016–2021, Remote Sens. Environ., 284, 113333, doi:10.1016/j.rse.2023.113333, 2023.

Wang, W., and Wu, Z.: Coastal dune rock development and Holocene climate changes in South China, J. Geogr. Sci., 20, 469–480, doi:10.1007/s11442-010-0469-8, 2010.

Wang, X., Zhou, M., and Xia, Y.: Evolution of China's coastal economy since the Belt and Road Initiative based on nighttime light imagery, Sustainability, 16, 1001, doi:10.3390/su16031001, 2024.

610 Wang, Z., Fang, Z., and Chang, J.: A two-step approach to extracting sandy beaches through integrating spatial semantic information from open-source geospatial datasets, Trans. GIS, 28, 2379–2396, doi:10.1111/tgis.13238, 2024.

Wei, X., Zheng, W., and Xi, C.: Shoreline classification in SAR image based on advanced geometric active contour model, Remote Sens., 13, 641, doi:10.3390/rs13040641, 2021.

Xiao, X., and Liang, S.: Assessment of snow cover mapping algorithms from Landsat surface reflectance data and application 615 to automated snowline delineation, Remote Sens. Environ., 307, 113444, doi:10.1016/j.rse.2024.113444, 2024.

Xu, N., Wang, L., and Xu, H.: Deriving accurate intertidal topography for sandy beaches using ICESat-2 data and Sentinel-2 imagery, J. Remote Sens., 4, 100041, doi:10.34133/remotesensing.100041, 2024.

Xu, X.: China GDP spatial distribution kilometer grid dataset, Resour. Environ. Sci. Data Center, doi:10.12078/2017121102, 2017.

620 Xu, X.: China population spatial distribution kilometer grid dataset, Resour. Environ. Sci. Data Center, doi:10.12078/2017121101, 2017.

Yang, J., and Huang, X.: The 30 m annual land cover dataset and its dynamics in China from 1990 to 2019, Earth Syst. Sci. Data, 13, 3907–3925, doi:10.5194/essd-13-3907-2021, 2021.

Yasir, M., Sheng, H., and Fan, H.: Automatic coastline classification and changes analysis using remote sensing and GIS 625 technology, IEEE Access, 8, 180156–180170, doi:10.1109/ACCESS.2020.3027883, 2020.

Yong, S. Y., O'Grady, J., and Gregory, R.: Regional-scale image segmentation of sandy beaches in southeastern Australia, Remote Sens., 16, 3159, doi:10.3390/rs16183159, 2024.

Zhang, H., Tian, P., and Zhong, J.: Mapping photovoltaic panels in coastal China using Sentinel-1 and Sentinel-2 images and Google Earth Engine, Remote Sens., 15, 3739, doi:10.3390/rs15153739, 2023.

630 Zhang, L., Fang, C., and Zhao, R.: Spatial-temporal evolution and driving force analysis of eco-quality in urban agglomerations in China, Sci. Total Environ., 866, 161465, doi:10.1016/j.scitotenv.2023.161465, 2023.

Zhang, L., Li, G., and Liu, S.: Spatiotemporal variations and driving factors of coastline in the Bohai Sea, J. Ocean Univ. China, 21, 1517–1528, doi:10.1007/s11802-022-5148-4, 2022.

Zhang, Q., Li, B., and Thau, D.: Building a better urban picture: Combining day and night remote sensing imagery, Remote
635 Sens., 7, 11887–11913, doi:10.3390/rs70911887, 2015.

Zhang, X., Liu, L., and Wu, C.: Development of a global 30 m impervious surface map using multisource and multitemporal remote sensing datasets with the Google Earth Engine platform, Earth Syst. Sci. Data, 12, 1625–1648, doi:10.5194/essd-12-1625-2020, 2020.

Zhang, X., Xu, M., and Wang, S.: Mapping photovoltaic power plants in China using Landsat, random forest, and Google
640 Earth Engine, Earth Syst. Sci. Data, 14, 3743–3755, doi:10.5194/essd-14-3743-2022, 2022.

Zhou, L., Yang, Y., and Li, G.: OSL dating of coastal dunes on the southeastern coast of Hainan Island, China, Front. Mar. Sci., 10, 1180635, doi:10.3389/fmars.2023.1180635, 2023.

Zhou, Y., Feng, X., and Liu, M.: Influence of beach erosion during wave action in designed artificial sandy beach using XBeach model: Profiles and shoreline, J. Mar. Sci. Eng., 11, 934, doi:10.3390/jmse11050934, 2023.

645 Zhu, Y., Li, Z., and Zhao, Z.: Spatio-temporal changes of coastline in Jiaozhou Bay from 1987 to 2022 based on optical and SAR data, Front. Mar. Sci., 10, 1206576, doi:10.3389/fmars.2023.1206576, 2023.

Zhao, Z., Chen, Y., Li, K., Ji, W., and Sun, H.: Extracting photovoltaic panels from heterogeneous remote sensing images with spatial and spectral differences, IEEE J. Sel. Top. Appl. Earth Obs. Remote Sens., 17, 5553-5564, doi:10.1109/JSTARS.2024.3369660, 2024.

650 Zou, Z., Xiao, X., and Dong, J.: Divergent trends of open-surface water body area in the contiguous United States from 1984 to 2016, Proc. Natl. Acad. Sci. U. S. A., 115, 3810–3815, doi:10.1073/pnas.1719275115, 2018.